




Article

# Orogenic Gold in Transpression and Transtension Zones: Field and Remote Sensing Studies of the Barramiya–Mueilha Sector, Egypt

Basem Zoheir <sup>1,2,\*</sup>, Mohamed Abd El-Wahed <sup>3</sup> , Amin Beiranvand Pour <sup>4,5</sup>  and Amr Abdelnasser <sup>1</sup> 

<sup>1</sup> Geology Department, Faculty of Science, Benha University, Benha 13518, Egypt; amr.khalil@fsc.bu.edu.eg

<sup>2</sup> Institute of Geosciences, University of Kiel, Ludewig-Meyn Str. 10, 24118 Kiel, Germany

<sup>3</sup> Tanta University, Geology Department, Faculty of Science, Tanta 31527, Egypt; mohamed.abdelwahad@science.tanta.edu.eg

<sup>4</sup> Korea Polar Research Institute (KOPRI), Songdomirae-ro, Yeonsu-gu, Incheon 21990, Korea; beiranvand.amin80@gmail.com

<sup>5</sup> Institute of Oceanography and Environment (INOS), Universiti Malaysia Terengganu (UMT), 21030 Kuala Nerus, Terengganu, Malaysia

\* Correspondence: basem.zoheir@ifg.uni-kiel.de or basem.zoheir@fsc.bu.edu.eg; Tel.: +49-177-210-4494

Received: 17 July 2019; Accepted: 10 September 2019; Published: 12 September 2019



**Abstract:** Multi-sensor satellite imagery data promote fast, cost-efficient regional geological mapping that constantly forms a criterion for successful gold exploration programs in harsh and inaccessible regions. The Barramiya–Mueilha sector in the Central Eastern Desert of Egypt contains several occurrences of shear/fault-associated gold-bearing quartz veins with consistently simple mineralogy and narrow hydrothermal alteration haloes. Gold-quartz veins and zones of carbonate alteration and listvenitization are widespread along the ENE–WSW Barramiya–Um Salatit and Dungash–Mueilha shear belts. These belts are characterized by heterogeneous shear fabrics and asymmetrical or overturned folds. Sentinel-1, Phased Array type L-band Synthetic Aperture Radar (PALSAR), Advanced Space borne Thermal Emission and Reflection Radiometer (ASTER), and Sentinel-2 are used herein to explicate the regional structural control of gold mineralization in the Barramiya–Mueilha sector. Feature-oriented Principal Components Selection (FPCS) applied to polarized backscatter ratio images of Sentinel-1 and PALSAR datasets show appreciable capability in tracing along the strike of regional structures and identification of potential dilation loci. The principal component analysis (PCA), band combination and band ratioing techniques are applied to the multispectral ASTER and Sentinel-2 datasets for lithological and hydrothermal alteration mapping. Ophiolites, island arc rocks, and Fe-oxides/hydroxides (ferrugination) and carbonate alteration zones are discriminated by using the PCA technique. Results of the band ratioing technique showed gossan, carbonate, and hydroxyl mineral assemblages in ductile shear zones, whereas irregular ferrugination zones are locally identified in the brittle shear zones. Gold occurrences are confined to major zones of fold superimposition and transpression along flexural planes in the foliated ophiolite-island arc belts. In the granitoid-gabbroid terranes, gold-quartz veins are rather controlled by fault and brittle shear zones. The uneven distribution of gold occurrences coupled with the variable recrystallization of the auriferous quartz veins suggests multistage gold mineralization in the area. Analysis of the host structures assessed by the remote sensing results denotes vein formation spanning the time–space from early transpression to late orogen collapse during the protracted tectonic evolution of the belt.

**Keywords:** Advanced Space borne Thermal Emission and Reflection Radiometer (ASTER); Sentinel 2; Synthetic Aperture Radar (SAR) data; Egyptian Eastern Desert; gold mineralization; structural control; transpression and transtension zones

## 1. Introduction

Remote sensing satellite imagery has a high capability of providing a synoptic view of geological structures, alteration zones and lithological units in metallogenic provinces. Typically, application of multi-sensor satellite imagery can be considered as a cost-efficient exploration strategy for prospecting orogenic gold mineralization in transpression and transtension zones, which are located in harsh regions around the world [1–13]. Synthetic Aperture Radar (SAR) is an active microwave remote sensing sensor that transmits and detects radiation with wavelengths between 2.0 and 100 cm, typically at 2.5–3.8 cm (X-band), 4.0–7.5 cm (C-band), and 15.0–30.0 cm (L-band) [7]. Longer wavelengths (L-band) can enhance the depth of penetration of radar signals through the Earth's surface and therefore provide valuable information for structural geology mapping related to orogenic gold mineralization [8,9]. The C-band and L-band SAR data, i.e., the Sentinel-1 and Phased Array type L-band Synthetic Aperture Radar (PALSAR) data, have successfully promoted mapping of structural lineaments that are associated with hydrothermal gold mineralization in tropical, arid, and semi-arid environments [4,14–18].

The hydrothermal alteration zones are normally impregnated with iron oxides, clay and carbonate  $\pm$  sulfate, which have diagnostic spectral signatures in the visible, near infrared, and shortwave infrared radiation regions [19]. The electronic processes caused by the transitional elements in these minerals, such as  $\text{Fe}^{2+}$ ,  $\text{Fe}^{3+}$ , Mn, Cr, Co and Ni, produces absorption features in the visible near infrared region (VNIR) (0.4 to 1.1  $\mu\text{m}$ ) [19]. The hydrous mineral phases with the OH groups (Mg–O–H, Al–O–H, Si–O–H) and  $\text{CO}_3$  acid group have diagnostic absorption features in short wave infrared region (SWIR) (2.0–2.50  $\mu\text{m}$ ) [20,21]. Using data of multispectral and hyperspectral remote sensing sensors for lithological and mineralogical mapping in metallogenic provinces have been continually demonstrated around the world [6,22–24]. The Advanced Space-borne Thermal Emission and Reflection Radiometer (ASTER) and Sentinel-2 data have high capabilities in discriminating lithological units and alteration zones associated with hydrothermal ore deposits using the VNIR and SWIR spectral data [11–13,25–27].

The Central Eastern Desert (CED) of Egypt is built up mainly of tectonized ophiolites, metasedimentary rock successions, granitoid intrusions, and subordinate volcanic rocks and molasse sediments generally of Neoproterozoic age [28]. Gold–quartz veins cutting mainly through the metavolcanic–metasedimentary rock successions or in small granitic intrusions have been intensely mined out and produced gold during ancient times [29]. Gold mineralization is thought to have occurred during episodes of calc-alkaline granite magmatism in the evolution of the Eastern Desert shield [30–32]. Shear-related gold lodes have been described in several occurrences in the South and Central Eastern Desert (SED, CED) [33–38]. Zoheir [39] discussed the possibility of temporal and spatial relationships between discrete gold occurrences and regional transpression shear zones particularly between the ophiolite and island arc terranes. The Au–quartz veins are typically hosted by brittle–ductile ductile and fault zones attributed to post-accretionary, wrench-dominated deformation [40,41].

In this study, Sentinel-1, PALSAR, ASTER, and Sentinel-2 data are analyzed to decode the distribution of geological structures and hydrothermal alteration zones associated with gold–quartz veins in the Barramiya–Mueilha Sector of the CED (Figure 1). This contribution comes in response to the present-day surge in gold exploration in the Eastern Desert of Egypt and other parts of the Nubian Shield (i.e., Sudan, Arabia, Eritrea, and Ethiopia). The main objectives of this study are: (i) To map the major lineaments, curvilinear structures, and intersections in the study area using Sentinel-1 and PALSAR datasets by employing the Feature-oriented Principal Components Selection (FPCS) technique; (ii) to identify the alteration zones and lithological units in association with brittle and ductile shear zones by applying principal component analysis (PCA), band combination and specialized band ratioing techniques to ASTER and Sentinel-2 datasets; (iii) to integrate field, structural analysis, and multi-sensor satellite imagery for an ample understanding of the setting and structural controls of gold occurrences in the study area; and (iv) to inaugurate a cost-effective multi-sensor satellite imagery approach for orogenic gold in transpression and transtension zones in the Egyptian Eastern Desert and analogous areas.

## 2. Geologic Setting

The Neoproterozoic shield rocks of the western part of the CED is dominated by dismembered ophiolites, tectonic mélangé of allochthonous blocks of serpentinite incorporated and intermixed with an intensively deformed pelitic and calcareous schists, locally with intercalations of quartzite and black marble bands [42]. In the Barramiya–Mueilha sector (Figure 1), serpentinite represents greenschist facies metamorphosed cumulus ultramafic rocks of an ophiolite sequence [43–46]. The island arc metavolcanic rocks in the study area (Figure 1) comprise metabasalt, basaltic meta-andesite, interbedded with dactylic tuffs and agglomerate, with accidental carbonate fragments. In the Wadi Dungash area, the island arc assemblages comprises mainly medium- to fine-grained, massive or foliated metabasalt and meta-andesite and epidote-chlorite schist. Pillowed morphologies are commonly observed in exposures of the less tectonized metabasalt in the area between Wadi Dungash and Wadi Barramiya [47]. Metagabbro-diorite complexes are weakly deformed rocks underlying extensive areas around Wadi Beizah. Large sub-rounded masses and discrete elongate masses of tonalite and granodiorite cut the ophiolitic mélangé, island arc rocks, and the syn-orogenic granitoids in the northern part of the study area. The late- or post-orogenic intrusions are mainly alkali-feldspar granites, granite porphyries, and less commonly albitite, i.e., the G. Mueilha (Figure 1).

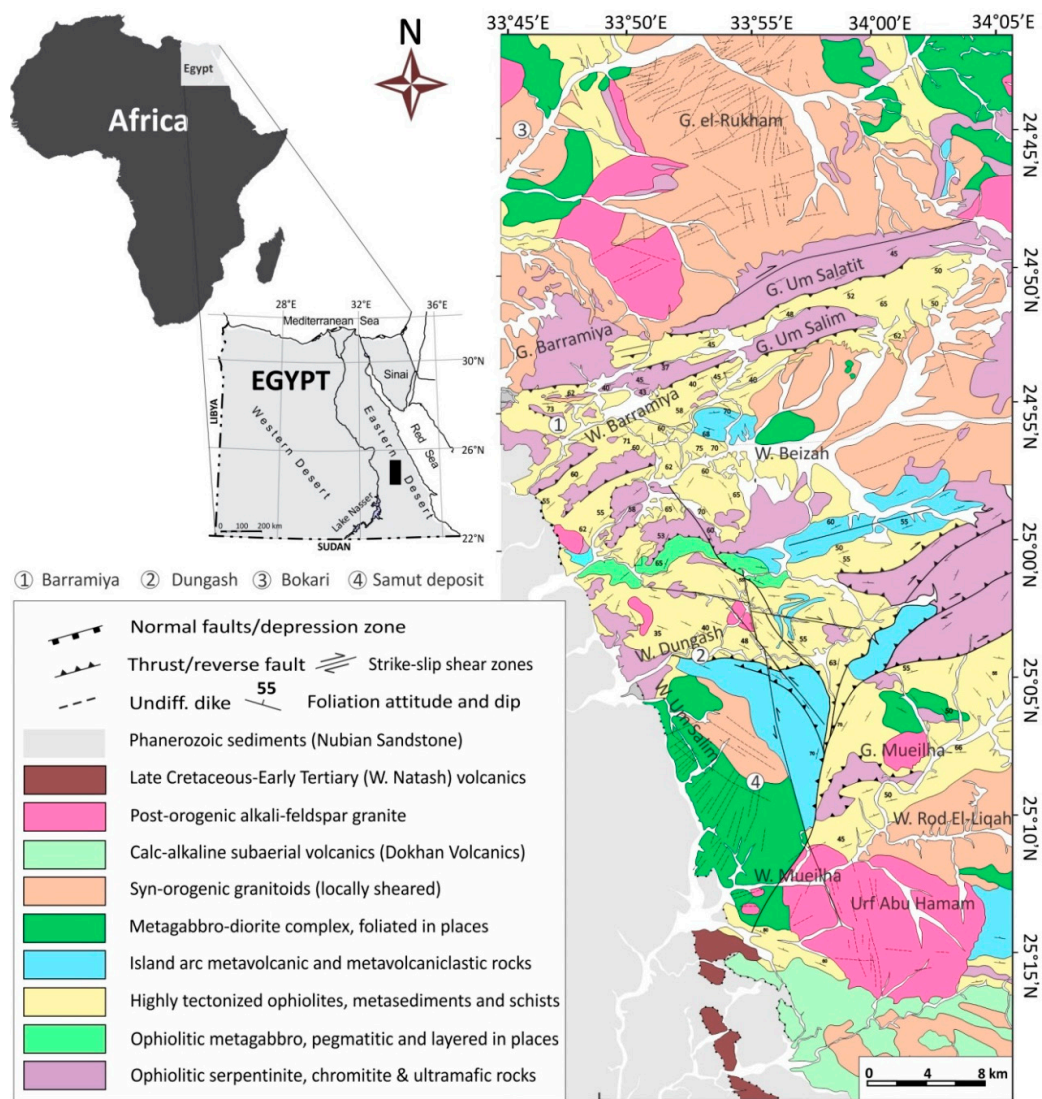


**Figure 1.** Simplified geological map of the Barramiya–Mueilha sector in the western part of the Central Eastern Desert of Egypt. Compiled from [35,36,44–47] and modifications based on new field verifications. Insets show the location of Egypt in Africa and the study area in Egypt.

Oval shaped and elongate masses of late- or post-tectonic granites cut the ophiolitic mélange, arc metavolcanics, and metagabbro-diorite rocks in the western and northern parts of the study area. These intrusions are cut by a system of NW- and NE-trending faults and shear zones. The Gabal Mueilha albite granite intrusion is known for historical economic Sn resources [48,49]. It exhibits sharp contacts with the country rocks and is intersected by NE and NW-trending faults/fracture sets filled by dikes and pegmatite veins. Rhyodacite–rhyolite rocks and their subvolcanic equivalents form a small exposure in the extreme southern part of the study area. The subvolcanic rocks are less deformed relative to the surrounding rocks and occur at the fault intersection zones [50,51]. Numerous sets of basaltic and dacitic dikes cut the granitoid rock terranes in different directions. The dominance of the ENE-trending dikes in the northern part of the study area adjacent to the ENE–WSW Barramiya–Um Salatit belt. The ~NNW-trending dikes in the south may imply different timing and geometry of the tensile deformation in the tectonic evolution of the area. The Barramiya–Mueilha sector contains several gold deposits that show ostensible features of structural control and association with hydrothermal carbonate zones.

### 3. Materials and Methods: SAR and Multispectral Satellite Data

#### 3.1. Data Characteristics

Sentinel-1, Phased Array type L-band Synthetic Aperture Radar (PALSAR), Advanced Space borne Thermal Emission and Reflection Radiometer (ASTER), and Sentinel-2 datasets were used for this study. Sentinel-1 is a C-band synthetic aperture radar (SAR) instrument (frequency = 5.40 gigahertz) with a spatial resolution of down to 5 m and an up to 400 km-wide swath. Sentinel-1 was launched on 3 April 2014 ([www.esa.int/copernicus](http://www.esa.int/copernicus)). It has four operational modes, namely (i) Strip Map (SM) mode with  $5 \times 5$  m spatial resolution and a 80 km swath, (ii) Interferometric Wide Swath (IW) mode with  $5 \times 20$  m spatial resolution and a 250 km swath, (iii) Extra Wide Swath (EW) mode with  $25 \times 100$  m spatial resolution and a 400 km swath, and (iv) Wave (WV) mode with  $5 \times 20$  m resolution and a low data rate ( $20 \times 20$  km images along the orbit every 100 km) [52,53]. Sentinel-1 contains single polarization (VV or HH) for the Wave mode and dual polarization (VV + VH or HH + HV) for all other modes [54]. In this study, Sentinel-1 Wave Mode data (Granule ID: S1B\_IW\_GRDH\_1SDV\_20181130T154622\_20181130T154647\_013836\_019A55, acquired on November 30, 2018) were obtained from the European Space Agency (ESA).

PALSAR sensor is L-band (1.27 gigahertz) synthetic aperture radar, and has a multi-mode observation function, which enables Fine, Direct Downlink, ScanSar, and Polarimetric modes. It contains multi-polarization configurations, namely HH, VV, HV, and VH, with variable off-nadir angles between 9.9 to 50.8 degrees, and different spatial resolutions of 10 m (Fine mode), 30 m (Polarimetric), and 100 m (ScanSar mode). The swath width is 30 km for the Polarimetric mode, 70 km for the Fine mode, and 250–350 km for the ScanSar mode [55–57]. A PALSAR scene covering the study area was acquired from the Earth and Remote Sensing Data Analysis Center (ERSDAC) Japan (<http://gds.palsar.ersdac.jspacesystems.or.jp/e/>). It was a Fine Mode Dual polarization (FBD) of HH + HV Level 1.5 product (ALPSRP080050480) acquired on 26 July 2007. The scene was of good quality (12.5 m pixel spacing), with an off-nadir angle of 34.3 and an incident angle of 38.8 degree, and was already geo-referenced to the UTM Zone 36 North projection with the WGS-84 datum.

ASTER is a multispectral sensor with 14 spectral bands, including three visible and near infrared radiation bands (VNIR; 0.52 to 0.86  $\mu\text{m}$ ) with a spatial resolution of 15 m, six shortwave infrared radiation bands (SWIR; 1.6 to 2.43  $\mu\text{m}$ ) with a spatial resolution of 30 m, and five thermal infrared radiation bands (TIR; 8.125 to 11.65  $\mu\text{m}$ ) with a spatial resolution of 90 m. A cloud-free, level 1T ASTER scene (AST\_L1T\_00303112003083059) of the study area was obtained from the U.S. Geological Survey Earth Resources Observation and Science Center (EROS) (<https://earthexplorer.usgs.gov/>). The scene was acquired on 11 March 2003 and was georeferenced to the UTM zone 36 North projection using the WGS-84 datum.



Sentinel-2 is multispectral sensor, launched on 23 June 2015, and provides 13 spectral bands, comprising of four bands in the VNIR region (0.45 to 0.66  $\mu\text{m}$ ), three narrow red edge bands (0.70 to 0.78  $\mu\text{m}$ ), two narrow NIR bands (0.84 to 0.86  $\mu\text{m}$ ) and two bands in SWIR region (1.6 to 2.20  $\mu\text{m}$ ), with spatial resolution ranging from 10, 20–60 m) with large swath width of 290 km [58,59]. In this study, a cloud-free, level-1 C Sentinel-2 (Granule ID: S2B\_MSIL1C\_20181207T082329\_N0207\_R121\_T36RWN\_20181207T120140, acquired on 7 December 2018) was obtained from the European Space Agency (ESA) (<https://scihub.copernicus.eu/>).

Processing of the different multispectral and radar data was made by using various software including the ENVI®(version 5.2, developed by L3Harris.com) and ArcGIS (version 10.3, developed by esri.com) packages.

### 3.2. Pre-Processing Methods

In this study, the Enhanced Lee filter was used to reduce speckle in Sentinel-1 and PALSAR radar imagery though concurrently conserving the texture evidence [60]. The Enhanced Lee filter is a revision of the Lee filter and likewise uses coefficient of variation within separate filter spaces [61,62]. The Enhanced Lee filter parameters used in this analysis are  $7 \times 7$  m filter size, 1.00 damping factor, and the coefficient of variation in cutoffs for homogenous and heterogenous areas were arranged as 0.5230 and 1.7320, respectively. Every pixel is placed by applying the Enhanced Lee filter in one of the following three classes: (i) Homogeneous class—pixel value is replaced by the average of the filter window; (ii) heterogeneous treatment—pixel value is substituted by a weighted mean; and finally (iii) point target class—pixel value remains unchanged.

The atmospheric correction is used to minimize the influences of atmospheric factors in multispectral data. The Internal Average Relative Reflection (IARR) method was applied to the ASTER and Sentinel-2 data. The IARR technique for mineral mapping requires no prior knowledge of the geological features [63]. The IARR normalizes the images to a scene with an average spectrum. The 30 m-resolution ASTER SWIR bands were re-sampled to match with the VNIR 15-m. Sentinel-2 bands were geo-referenced to the zone 36 North UTM projection using the WGS-84 datum and the spectral bands were stacked on the 10-meter resolution bands via the nearest neighbor resampling method to preserve the original pixel values.

### 3.3. Image Processing Methods

The inverse relationship of HH or VH and HV or VV polarizations of the SAR data can optimize the geological features with different orientations. This is principally useful for the topographic applications and mapping structural pattern [4]. The combination of the different polarizations (HH or VH and HV or VV) results in numerous cross-polarized backscatter ratio pictures. In this study, ratio images of VV, VH, VH/VV and VH + VV of Sentinel-1 and HV, HH, HH/HV and HH + HV of PALSAR were produced. We used the Feature-oriented Principal Components Selection (FPCS) technique to analyze the backscatter ratio polarization images of Sentinel-1 and PALSAR datasets [64,65]. We assessed the PCA eigenvector loadings on the basis of correlation matrix in order to choose the most suitable PC which ascertains the important backscatter signatures and variability. A correlation matrix is normally used if the variances of individual variates are high, or if the units of measurement of the individual variates differ. The factor model is based on summarizing the total variances. Unities are used in the diagonal of the correlation matrix for PCA to imply that all variance is common or shared. Whether a surface feature appears as dark or bright pixels, it is based on the sign of the eigenvector loadings, coupled with the effect of topographic perception on the radar backscatter response [65]. Consistent improvements in image enhancement and signal to noise ratio (SNR) are possible by using a correlation matrix in the principal component analysis [4]. The computed correlation eigenvector values for Sentinel-1 and PALSAR datasets are shown Tables 1 and 2, respectively.

**Table 1.** Eigenvector matrix of copolarized and cross-polarized backscattering for Sentinel-1 Feature-oriented Principal Components Selection (FPCS) images.

Eigenvector	VH	VV	VH/VV	VH + VV
FPCS 1	0.230369	0.563194	0.563194	0.563194
FPCS 2	0.783316	−0.591162	0.591162	0.591162
FPCS 3	−0.003523	−0.003523	0.999990	0.999990
FPCS 4	−0.999990	−0.577350	−0.000000	0.577350

VH = vertical horizontal, VV = vertical vertical.

**Table 2.** Eigenvector matrix of copolarized and cross-polarized backscattering for PALSAR FPCS images.

Eigenvector	HH	HV	HH/HV	HH + HV
FPCS 1	0.589359	0.194688	0.004823	0.784047
FPCS 2	−0.564816	0.792703	−0.025923	0.227887
FPCS 3	0.017490	−0.019617	−0.999652	−0.002127
FPCS 4	−0.577350	−0.577350	0.000000	0.577350

HH = horizontal horizontal, HV = horizontal vertical.

The principal component analysis (PCA), band combination and specialized band ratios techniques were applied to ASTER and Sentinel-2 data to extract information related to lithological and hydrothermal alteration mapping. The PCA is a standard statistical method applied to minimize the independent principal components and highlight most of the variability inherited from the numerous combined band images [66,67]. In this study, the PCs are calculated using the covariance matrix (scaled sums of squares and cross products) of ASTER VNIR + SWIR and Sentinel-2 spectral bands. Sentinel-2 bands 1, 9, and 10 were excluded from this analysis as they do not contain mineralogical/geological information. These bands contain information related to atmospheric issues (e.g., aerosol scattering, water vapor absorption, and detection of thin cirrus) irrelevant to this study [64]. The eigenvector matrix for the ASTER and Sentinel-2 data derived from the PCA are given in Tables 3 and 4.

The PCA is capable of determining the direction of space containing the highest sample variance, and moving on to the orthogonal subspace in this direction to find the next highest variance. The result is iteratively discovering an ordered orthogonal basis of the highest variance. The subspace defined by the first  $n$  PCA vectors can explain a given percentage of the variance. The subspace of dimension  $n$  explains the largest possible fraction of the total variance [66]. The PCA1 contains the albedo is related largely to the topographic features. Three first PCA images (PCA1, PCA2, and PCA3), containing the highest topographical and spectral information, are suitable for lithological discrimination. The PCA images (except PCA 1) may have information related to alteration minerals, which could be reproduced in the eigenvector loading of the absorption and reflection bands. A PC image with moderate to high eigenvector loadings for the indicative bands (reflection and/or absorption bands) and opposite signs promotes an efficient discrimination of a given mineral. If the loading in the reflection band of a given mineral is positive, the enhanced pixels related to the mineral will appear as bright pixels. On the contrary, the enhanced related pixels will appear as dark if the loading to a given mineral in the reflection band is negative [67]. For inverting the dark pixels to bright pixels, negation can be accomplished by multiplication by  $-1$ .

**Table 3.** Eigenvector matrix for Advanced Space-borne Thermal Emission and Reflection Radiometer (ASTER) visible near infrared region (VNIR) + short wave infrared region (SWIR) principal component analysis (PCA) images.

Eigenvector	Band 1	Band 2	Band 3	Band 4	Band 5	Band 6	Band 7	Band 8	Band 9
PCA 1	-0.286530	-0.343729	-0.329190	-0.329130	-0.309398	-0.316583	-0.363650	-0.381071	-0.331134
PCA 2	0.549949	0.503725	0.370167	-0.145513	-0.182937	-0.175862	-0.266600	-0.302618	-0.242021
PCA 3	-0.226565	0.135415	0.271478	-0.498784	-0.406829	-0.358883	0.207509	0.453128	0.255251
PCA 4	-0.608617	0.126442	0.533556	0.496999	-0.100609	-0.083579	-0.132278	-0.102609	-0.191767
PCA 5	-0.296023	0.110156	0.237883	-0.545338	0.291567	0.563536	-0.300481	-0.167608	0.159023
PCA 6	-0.023765	-0.166820	0.260418	-0.267115	0.557757	-0.291015	0.480996	-0.115227	-0.438202
PCA 7	0.126345	-0.329776	0.249486	0.076552	0.288319	-0.444288	-0.282746	-0.222119	0.630381
PCA 8	-0.297947	0.666275	-0.453618	0.008140	0.296406	-0.318394	0.056334	-0.184583	0.187068
PCA 9	0.027941	0.033903	-0.061731	0.005964	0.357891	-0.178985	-0.575640	0.650058	-0.283134

**Table 4.** Eigenvectors and eigenvalues of correlation matrix of Sentinel-2 PCA images.

Eigenvector	Band 2	Band 3	Band 4	Band 5	Band 6	Band 7	Band 8	Band 8a	Band 11	Band 12
PCA 1	-0.130767	-0.195965	-0.294453	-0.305036	-0.323206	-0.340531	-0.332815	-0.346959	-0.421500	-0.368126
PCA 2	0.219830	0.283259	0.314141	0.182452	0.160849	0.138366	0.241307	0.086667	-0.547330	-0.573705
PCA 3	-0.330657	-0.392816	-0.335883	0.295142	0.344046	0.361373	-0.324495	0.361036	-0.123340	-0.191365
PCA 4	-0.504592	-0.418581	0.185161	-0.229417	-0.109091	-0.024353	0.653589	0.124095	-0.162823	0.040942
PCA 5	-0.104777	-0.066455	0.061494	-0.025064	0.018281	-0.049037	0.088132	-0.110870	0.690943	-0.692817
PCA 6	0.250524	0.098325	-0.259140	-0.241083	-0.368827	-0.148165	0.049876	0.789284	0.055270	-0.125685
PCA 7	-0.074844	-0.061944	0.038226	0.476730	0.238402	-0.824566	0.033654	0.150443	-0.015442	0.032866
PCA 8	0.306221	-0.016038	-0.648371	-0.181613	0.458534	-0.044668	0.453038	-0.186550	-0.015476	-0.008441
PCA 9	-0.054521	0.038123	0.324790	-0.643651	0.579072	-0.165281	-0.282445	0.182228	-0.008348	0.010264
PCA 10	0.628125	-0.729531	0.263138	0.025161	-0.024824	0.011445	-0.046073	-0.021424	0.006267	-0.000219

Several ASTER VNIR + SWIR and Sentinel-2 band combinations and band ratio images are tested and adopted for mapping lithological units associated with gold occurrences in the study area. Band ratio technique is used for reducing the effects of topography and enhancing the spectral differences between bands. It is a technique where the digital number value of one band is divided by the digital number value of another band. Band ratios are very useful for emphasizing hydrothermal alteration minerals and lithological units. Dividing one spectral band by another produces an image that provides relative band intensities. The final goal is to minimize the illumination differences due to topography [68]. Ratio images can be meaningfully interpreted because they can be directly related to the spectral properties of minerals. Ratioing can enhance minor differences between minerals by defining the slope of spectral curve between two bands. The band ratio technique is, therefore, specifically applicable to highly exposed areas and rugged terrains in arid regions [6]. The ASTER band combination images (R:4, G:3, B:1) and (R:4, G:7, B:3) are processed to map  $\text{Fe}_2\text{O}_3/\text{MgO}$  and  $\text{Al}_2\text{O}_3$ -rich rocks in the study area. The Sentinel-2 band combination (R:11, G:8, B:2) and (R:11, G:12, B:7) images are generated to map  $\text{Fe}_2\text{O}_3/\text{MgO}$  and  $\text{Al}_2\text{O}_3$ -rich rocks [25]. The band ratio of ASTER bands, 4/2 (gossan), 4/3 (ferric oxide), (7+9)/8 (chlorite/epidote/clcrite) [68], are used here to highlight the distribution of ophiolitic and island arc rocks in the study area. The hydrothermal alteration zones are characterized by substantial contents of hydrous ferromagnesian silicate and iron oxides. The Sentinel-2 band ratios, 11/4 (gossan), 11/8a (ferric oxide), 12/11 (ferrous silicates) and 11/12 (hydroxyl alteration) are used to map the different rock units [59] and to emphasize on the hydrothermal alteration zones.

## 4. Results

### 4.1. Remote Sensing Data Analysis

Analyzing the eigenvector loadings for Sentinel-1 cross-polarized backscatter ratio images indicates that the FPCS2 has strong loadings of VH (0.783316) and VV (−0.591162) with opposite signs (Table 1). Cross polarization (VH) is extremely sensitive to geologic structures, while surface roughness is reflected in robust reflection and high VV backscatter [4]. The inverse relationship between the VH and VV loadings in the FPCS2 emphasizes the topographic features with different orientations, contrast, and textural signatures. Figure 2A,B shows the FPCS2 Sentinel-1 image-map of the selected spatial subset covering the study area. Structural elements related to the transtension and transpression zones are traceable in Figure 2A, and are annotated in Figure 2B. Well-developed foliations and shear cleavages are dominated in the transpression zone (ductile zone), while zones accommodating displacements and form discontinuities are considered as transtension zones. The ENE-striking foliation and related close and overturned folds extend for several kilometers and enfold the huge ophiolite blocks. A considerable difference in the topography and foliation trajectories in terranes of the ophiolite nappes relative to the island arc metavolcanic rocks emphasizes distinctive deformation histories, where shortening should have brought together tectonically different terranes now are juxtaposed.

The depth of penetration of radar signal is improved by using the L-band radar data, therefore, PALSAR data have the capability to map geological structures that may be covered by sand in arid regions. The FPCS technique is applied to cross-polarized backscatter ratio images of PALSAR, including HV, HH, HH/HV and HH + HV (Table 2). Different polarizations are sensitive to ground surface features of different dimensions; they collectively bring out greater geological–geomorphological–structural details [4]. Considering the eigenvector loadings for PALSAR cross-polarized backscatter ratio images, it is evident that the FPCS2 contains information for structural mapping and topographic enhancement due to the strong contribution of HH (−0.564816) and HV (0.792703) with opposite signs (Table 2). Figure 3A,B shows the FPCS2 PALSAR image-map of the selected spatial subset covering the study area. The FPCS2 image-map clearly discriminates the relatively high topographic, intensely sheared ophiolitic nappes from the tectonically underlying, low topographic, island arc metavolcanic and metavolcaniclastic rocks. Folding of the ophiolitic rocks appears to be more recognizable in the southern part than in the northern part of the study area. Typically, high brightness contrast, textural variability, and tonal variation are recorded in the FPCS2 PALSAR image-map compared to the Sentinel-1 images.



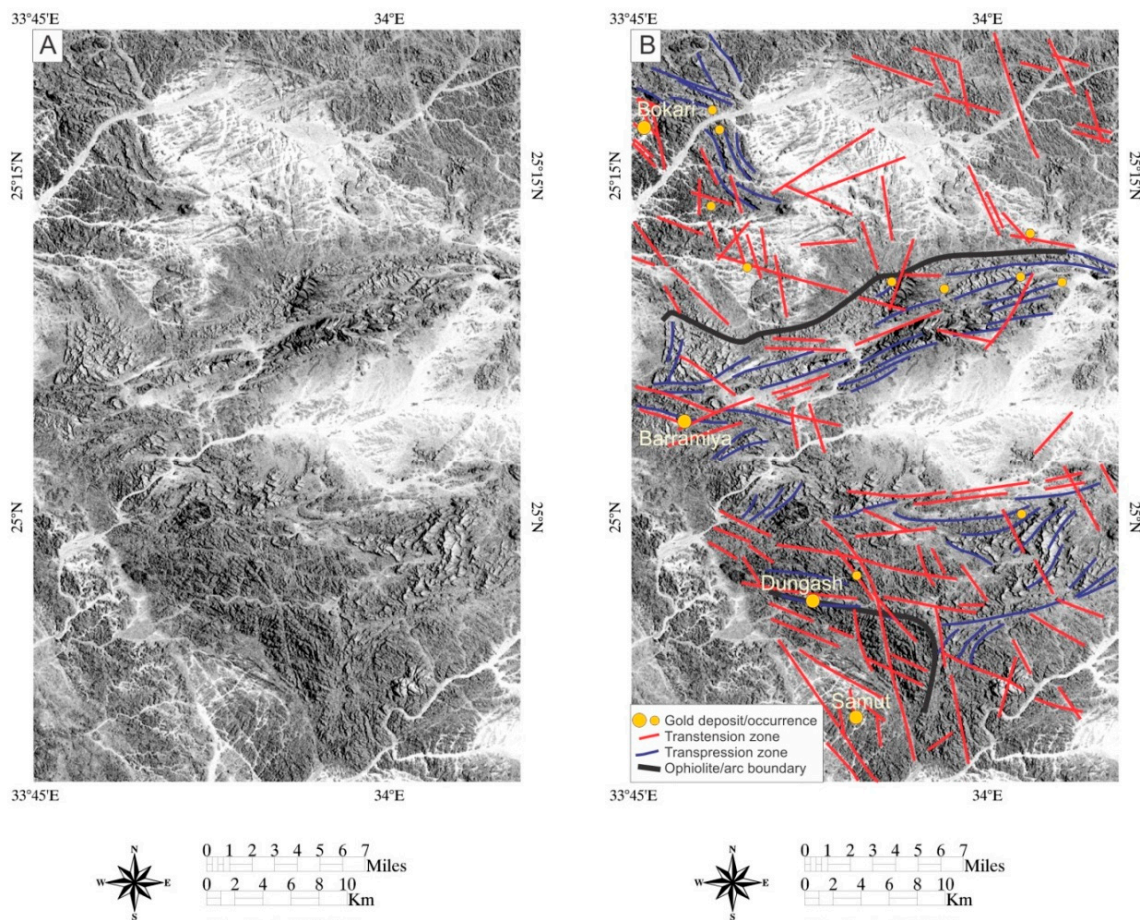


**Figure 2.** Processed Sentinel-1 data of the Barramiya–Mueilha area showing: (A) Feature-oriented Principal Components Selection (FPCS2) highlighting the variable styles of deformation in the study area. (B) Same as in A with interpreted structural elements and locations of gold deposits/occurrences. For more details please refer to the next sections.

A 9-band PCA is constructed from the original 9-band (VNIR + SWIR) of ASTER image covering the study area (Table 3). The PC1 band contains the largest percentage of data variance and albedo related to topographical features. The second and third PC bands contain the second largest data variance and spectral information. Thus, the first three high order PCs (1, 2, and 3) contain approximately 99% of spectral information, which can be used for lithological mapping rather than the subsequent low order principal components (4, 5, 6, etc.) which usually contain < 1% of spectral information and low signal-to-noise ratios. The last PCA bands may contain information related to alteration minerals or can appear noisy because they contain very little variance [4,11,12]. Accordingly, PC1, PC2, and PC3 can be considered in lithological mapping as Red–Green–Blue color composite, especially for arid region such study area. Figure 4A shows RGB color composite of the PC1, PC2, and PC3 for ASTER VNIR + SWIR bands covering the study area.

Most of the lithological units contain distinguishable spectral characteristics compliant with the geological map (Figure 1). However, the lithologies with analogous spectral features are hard to discriminate. The highly tectonized ophiolites, metasediments, and schists are expressed by yellow to orange pixels, demarcating the ductile shear zones in the central part of the study area (Figure 4A). Post-orogenic granites in the northwestern part of the study area appear as bluish green pixels, locally with pinkish yellow pixels. Spectral signature comparable to the granitic rocks are explained as alteration products of feldspar to clay minerals in brittle (transtension) shear zones. Metagabbro–diorite complex and the Nubian Sandstone appear as magenta to purple pixels. In Figure 4A, the ophiolitic rock terranes are notably separated from the island arc rocks by the pale green color, whereas the

island arc metavolcaniclastic rocks, with a reddish image signature, form an autochthonous block in the southwestern part of the area and is surrounded by major thrusts.

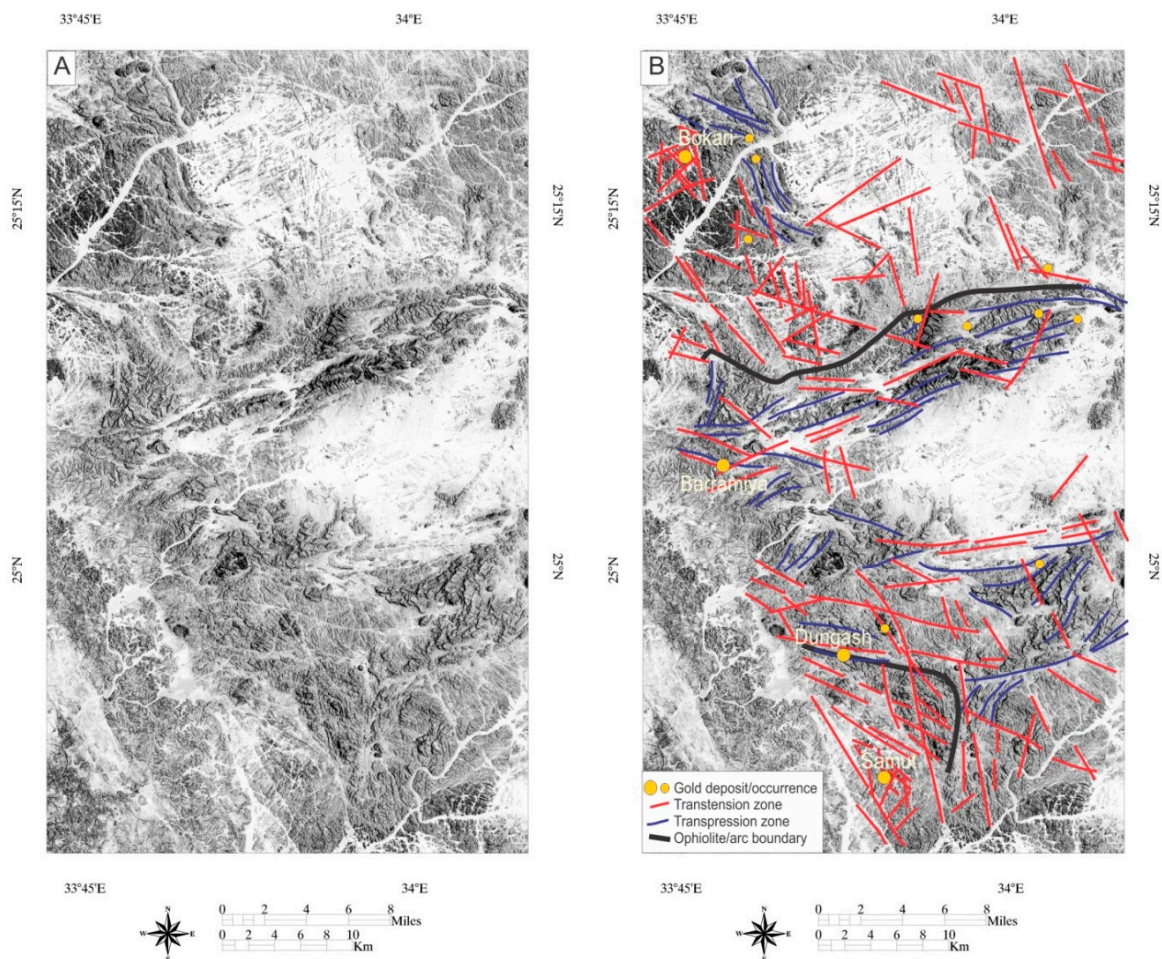


**Figure 3.** Processed Phased Array type L-band Synthetic Aperture Radar (PALSAR) data of the Barramiya–Mueilha area: (A) Feature-oriented Principal Components Selection (FPCS2) image showing fold traces and foliation trajectories most prominent in the central part of the area, (B) Same as A with interpreted structural elements and locations of gold deposits/occurrences. The different structural elements are classified based on fieldwork as detailed in the text.

Analysis of the eigenvector loadings for the ASTER VNIR + SWIR dataset shows that the PC4 has strong loadings of band 1 ( $-0.608617$ ) and band 4 ( $0.496999$ ) with opposite signs (Table 3). Hematite, jarosite, goethite, and limonite tend to have strong absorption features in  $0.4\text{--}1.1\ \mu\text{m}$ , coinciding with bands 1, 2, and 3 of ASTER, and high reflectance in  $1.56\text{--}1.70\ \mu\text{m}$ , coinciding with band 4 of ASTER [68,69]. Therefore, this PC image contains spectral information for mapping iron oxide/hydroxide minerals. The PC5 has high loadings of band 4 ( $-0.545338$ ) and band 6 ( $0.563536$ ) with opposed signs (Table 3). Al–OH mineral groups contain spectral absorption features in  $2.1\text{--}2.2\ \mu\text{m}$  and reflectance in  $1.55\text{--}1.75\ \mu\text{m}$ , which coincide with bands 5 and 6 ( $2.145\text{--}2.225\ \mu\text{m}$ ) and 4 ( $1.600\text{--}1.700\ \mu\text{m}$ ) of ASTER [69]. Accordingly, the PC5 can enhance kaolinite, alunite, and sericite (muscovite) mineral groups. It should be noted that the dark pixels in PC5 need to be inverted to bright pixels by negation. The PC6 shows strong positive loading in band 5 ( $0.557757$ ) and strong negative loading in band 9 ( $-0.438202$ ) (Table 3). Fe, Mg–OH-bearing alteration minerals and  $\text{CO}_3$  mineral groups show high absorption characteristics in the position defined by bands 8 and 9 ( $2.295\text{--}2.430\ \mu\text{m}$ ) and low absorption features in band 5 ( $2.145\text{--}2.185\ \mu\text{m}$ ) of ASTER [69]. So, the PC6 may have spectral information for mapping epidote, chlorite, and calcite. Figure 4B shows an RGB color composite



image of PC4 (R), PC5 (G), and PC6 (B) covering the study area. The red and magenta pixels have high surface abundance of iron oxide/hydroxide minerals, which are mostly associated with ophiolitic serpentinite, chromitite, and ultramafic rocks, highly tectonized ophiolites, metasediments and schists, and Nubian sandstone. The yellow pixels (admixture of iron oxide/hydroxide and Al–OH mineral groups) are typically occurred in alkali-feldspar granite and granitoids background (transtension zones). The green pixels are associated with Nubian sandstone, recent alluvium, ophiolitic serpentinite, chromitite and ultramafic rocks, syn-orogenic granitoids, and post-orogenic alkali-feldspar granites. The blue pixels strongly develop in the mafic and ultramafic rocks such as serpentinite, chromitite, and metagabbro-diorite complex (Figure 4B).

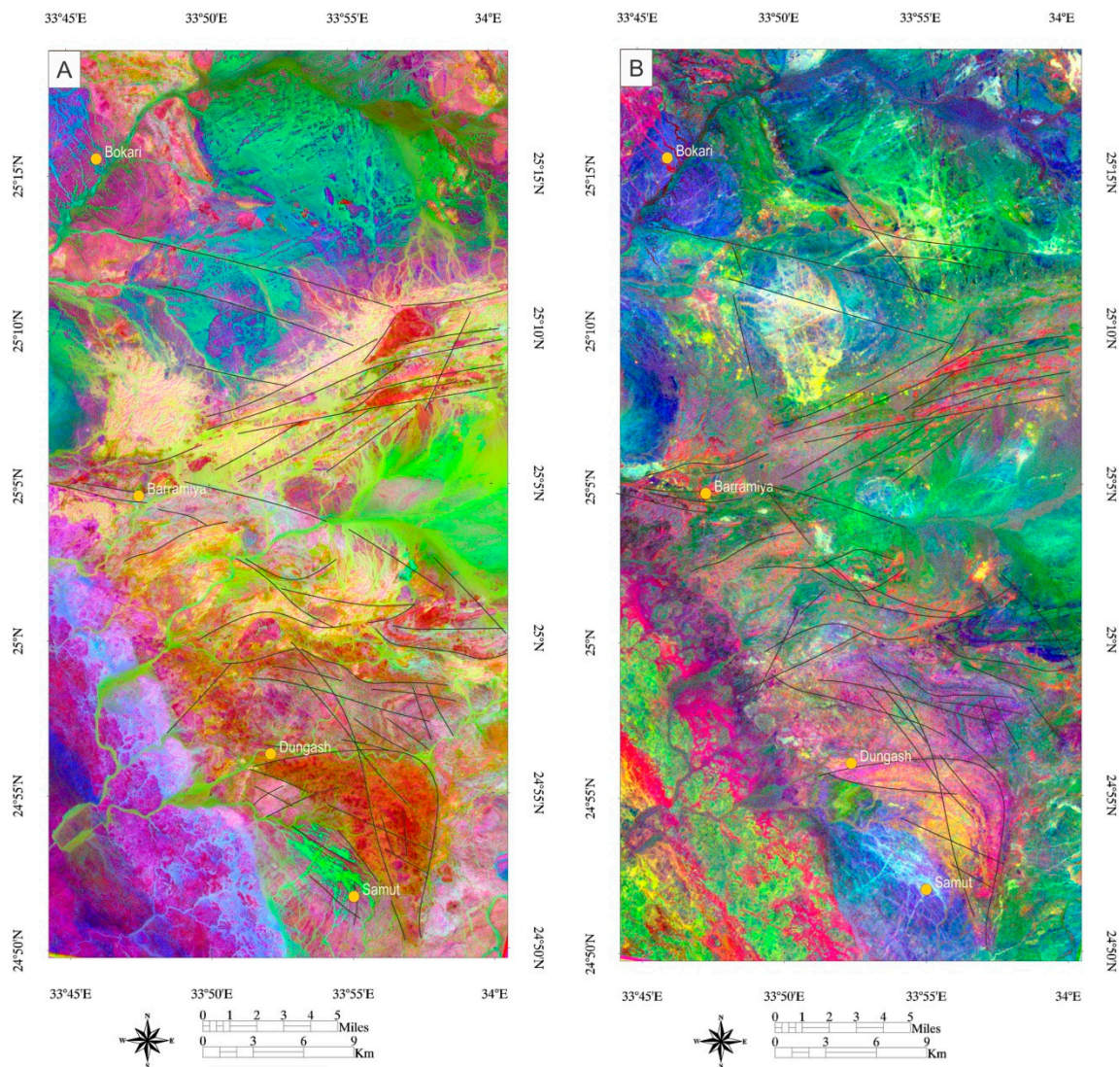


**Figure 4.** False-color composite, ASTER PCA images for the study area: (A) PC1, PC2, and PC3 (in RGB channels) shows the island arc metavolcanic/metavolcaniclastic rocks as red pixels, whereas the ophiolitic rocks and ophiolitic mélangé rocks exhibit a greenish image signature. The unconformity boundary is marked by the transition to pale blue areas (of the Nubian Sandstone) in the southwestern part of the area, (B) PC4, PC5, and PC6 (in RGB channels) differentiates the iron oxide/hydroxide minerals (red pixels), Al–OH mineral groups (green pixels) and Fe, Mg–OH-bearing alteration minerals and CO<sub>3</sub> mineral groups (blue pixels). Solid black lines refer to the main lineaments (i.e., fault and shear zones) in the area. Notice that the curvilinear morphologies of the lineaments (transpression zones) in the central part, whereas straight lineaments (herein classified as transtension zones) prevail in the northern and extreme southern parts of the area.



Figure 5A (PC1, PC2, and PC3) shows the island arc metavolcanic/metavolcaniclastic rocks as reddish pixels. The light green domains in the ophiolitic mélangé terranes are those which experienced high strain and demarcating transpression, which is highly tectonized ophiolites and schists as in the geological map. The boundary between ophiolites and island arc rocks appears prominent, and fold trajectories are easy to trace. The boundary between the Nubian sandstone and adjacent lithological units appear as light blue lines and changes into red and blue color towards the western part due to irregular abundance of ferrous silicates in this Phanerozoic sedimentary rocks. Post-orogenic alkali-feldspar granite and syn-orogenic granitoids represent in greenish-blue to blue color in northwestern part of the study area, while metagabbro–diomite complex depicts as magenta to light brown color (Figure 5A).

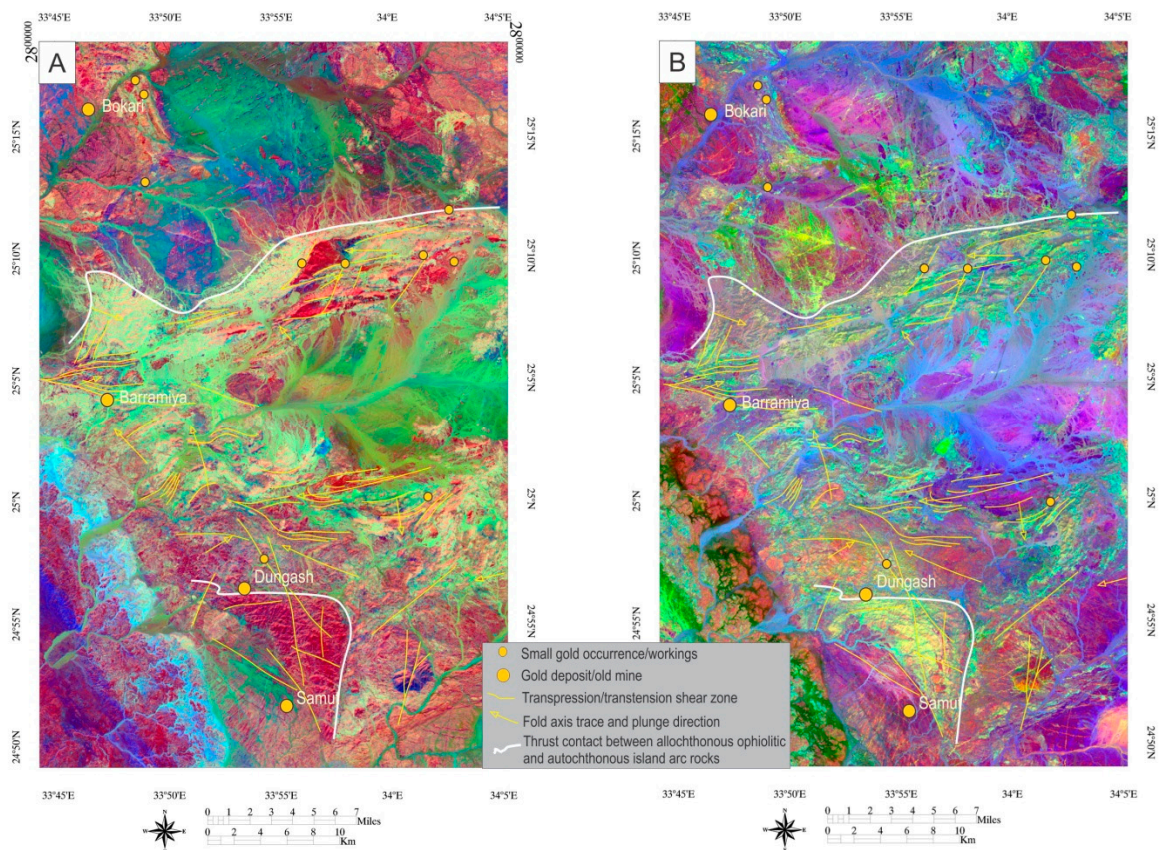


**Figure 5.** False-color composite, Sentinel-2 PCA images for the study area: (A) PC1, PC2, and PC3 in R, G, and B channels, respectively. Notice the island arc metavolcanic/metavolcaniclastic rocks are conspicuously distinctive as reddish color pixels. The light color domains within the ophiolitic mélangé terranes are those experienced high strain and demarcating transpression. The boundary between ophiolites and island arc rocks appears prominent and fold trajectories are easy to trace, (B) PC6, PC5, and PC4 in R, G, and B channels, respectively. Iron oxide/hydroxide minerals (red pixels), Al–OH and Fe, Mg–OH-bearing and CO<sub>3</sub> alteration minerals (green pixels) and ferrous silicates mineral groups (blue pixels). The yellow lines refer to the main structural elements (faults, thrusts, and shear zones), while the yellow arrows are traces of the fold axial planes and the arrowhead point towards the plunge direction.

The magnitude and sign of eigenvector loadings for Sentinel-2 (Table 4) reveal that the PC4 contains a strong negative loading for band 2 (−0.504592), a strong positive loading for band 8 (0.653589) and a moderate negative loading for band 11 (−0.162823). Ferrous silicates such as biotite, chlorite, and amphibole can be detected using band 2 (0.450–0.550 μm), band 8 (0.800–0.910 μm) and band 11 (1.520–1.850 μm) of Sentinel-2 due to their spectral features [25,27]. The PCA5 shows a strong loading for band 11 (0.690943) and band 12 (−0.692817) with opposite signs (Table 4). A PCA5 image can,



therefore, discriminate between the hydrous and intensely deformed ophiolitic mélange rocks from the island arc rocks. Compressional structures are conspicuous in the central part of the study area, where hydroxyl mineral zones prevail. The PCA6 has great contribution for band 6 (−0.368827) and band 8a (0.789284) with opposite signs and a moderate contribution for band 2 (0.250524) (Table 4). The PCA6 image contains important information about Fe-oxides/hydroxides that are mainly enriched in the ultramafic rocks, i.e., ophiolites. A RGB (PC6, PC5 and PC4) composite image (Figure 5B) shows the different lithological units and alteration zones with distinct image signatures. The areas with high abundance of hydrous minerals and Fe-oxides/hydroxides appear as yellow pixels exemplify the highly tectonized ophiolites and schists. The yellow pixels also represent the post-orogenic alkali-feldspar granite, syn-orogenic granitoids and island arc metavolcanic and metavolcaniclastic rocks. Intense foliation and shear cleavages by aligned hydrous minerals typify the ductile shear (transpression) zones. Carbonate alteration is also associated with the transpression zones. Ferrugination zones that are associated with faults/brittle shear (transtension) zones are commonly irregular in shape and scattered.

When comparing the Sentinel-2 image (Figure 5B) with the ASTER image (Figure 4B), the hydroxyl minerals and iron oxide/hydroxide zones are found better discriminated on the ASTER image. The ASTER spectral bands are particularly designed to depict the Al–OH, Fe, Mg–OH-bearing alteration and CO<sub>3</sub> mineral groups and iron oxide/hydroxides. Bands 11 and 12 of Sentinel-2 do not have enough spectral width for distinguishing specific Al–OH, Fe, Mg–OH and CO<sub>3</sub> mineral assemblages. Bands 2–9 (0.450–1.20 μm) of Sentinel-2 contain enough spectral and spatial data for mapping iron absorption feature parameters [25], and can therefore be used for detecting goethite, jarosite, and hematite. In the Sentinel-2 image (Figure 5B), mafic and ultramafic lithological units such as metagabbro–diorite complex appear as magenta pixels because of the high content of iron in their composition.

Figure 6A shows an ASTER RGB combination image of band 4 (R), band 3 (G), and band 1(B) for mapping Fe<sub>2</sub>O<sub>3</sub>/MgO-rich rocks in the study area. It demarcates ophiolitic serpentinite as dark pixels, whereas rocks with lesser contents of ferromagnesian minerals exhibit lighter image signatures. Post-orogenic alkali-feldspar granite and syn-orogenic granitoids appear in light pink to white due to the low contents of Fe<sub>2</sub>O<sub>3</sub> and MgO, while the mafic to ultramafic lithological units are expressed by dark green pixels (ophiolitic serpentinite, chromitite, and ultramafic rocks), green pixels (metagabbro–diorite complex) and brown to magenta pixels (the highly tectonized ophiolites and island arc metavolcanic and metavolcaniclastic rocks). Figure 6B displays an ASTER RGB combination image of band 4 (R), band 7 (G), and band 3 (B) for enhancing Al<sub>2</sub>O<sub>3</sub>-rich rocks. This image highlights post-orogenic alkali-feldspar granite, syn-orogenic granitoids and Nubian sandstone as green areas and carbonate alteration zones as greenish rafts in the high strain zones in the eastern part of the belt. The lithological units such as metagabbro–diorite complex and schists and metavolcaniclastic rocks contain moderate content of aluminosilicate minerals appear as dark green pixels. The ophiolitic serpentinite, chromitite, and ultramafic rocks and the highly tectonized ophiolites represent in black pixels attributed to very low content of Al<sub>2</sub>O<sub>3</sub> in their composition.

Figure 7A,B are Sentinel-2 RGB combination images of band 11 (R), band 8 (G), and band 2 (B) for mapping Fe<sub>2</sub>O<sub>3</sub>/MgO-rich rocks and band 11 (R), band 12 (G) and band 7 (B) for identifying Al<sub>2</sub>O<sub>3</sub>-rich rocks. Mafic mineral-rich rocks are clearly delineated in Figure 7A as dark green in color, including the ophiolitic serpentinite, chromitite, and ultramafic rocks and highly tectonized ophiolites. The metagabbro–diorite complex appears as green color because of a high to moderate contribution of ferromagnesian minerals. Moreover, the different content of ferromagnesian minerals in ophiolitic and island arc rocks promotes the ease differentiation based on RGB color composite (Figure 7A). The folded ophiolitic rocks are noticeably distributed adjacent to the variably deformed island arc rocks in the southern part of the study area. The Al<sub>2</sub>O<sub>3</sub>-rich rocks are enhanced in Figure 7B as green color. The post-orogenic alkali-feldspar granite and syn-orogenic granitoids, Nubian sandstone, metagabbro–diorite complex and island arc metavolcanic and metavolcaniclastic rocks depict as green color. However, ophiolitic serpentinite, chromitite and ultramafic rocks and highly tectonized

ophiolites only represent as black pixels. Compared to the Sentinel-2 image (Figure 7A,B), the ASTER RGB images (Figure 6A,B) are strongly capable of discriminating lithological units with different content of  $\text{Fe}_2\text{O}_3/\text{MgO}$  and  $\text{Al}_2\text{O}_3$ .

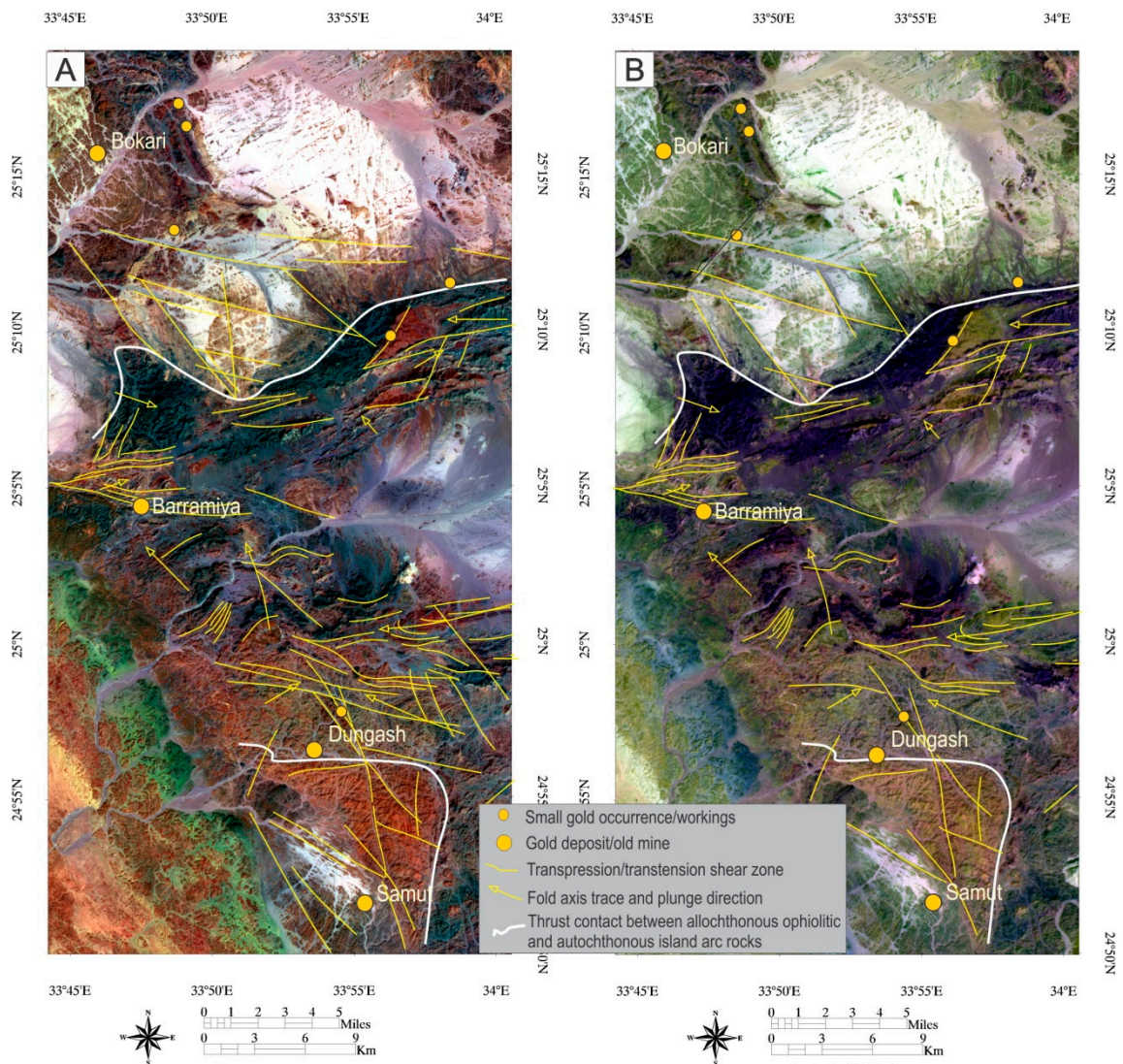


**Figure 6.** False-color composite, ASTER band combination images for the study area: (A) (R: Band 4, G: Band 3, B: Band 1) used to map  $\text{Fe}_2\text{O}_3/\text{MgO}$ -rich rocks, (B) (R: Band 4, G: Band 7, B: Band 3) used to enhance the signature of  $\text{Al}_2\text{O}_3$ -rich rocks to promote detailed mapping of the folded ophiolitic rocks.

Figure 8A–C are ASTER band ratio images for mapping gossan (4/2), ferric oxide (4/3), and the chlorite/epidote/calcite mineral group (7+9)/8. High digital number (DN) value pixels that appear as bright pixels indicate the spectral signatures of particular mineral or mineral groups [68,69]. Figure 8A shows the gossan zone as bright pixels, mostly associated with the highly tectonized ophiolites and schists, island arc metavolcanic and metavolcaniclastic rocks. The ferric oxide-rich zones are typically expressed by bright pixels in Figure 8B. The island arc rocks are seen as bright pixels in Figure 8C, most likely because of the abundant hydrous minerals such as mica, amphiboles, chlorite, and epidote. This observation ascertains that these rocks were tectonically overlain by thrust ophiolitic nappes. Talc carbonate and listvenite zones in the ophiolitic domains appear as bright zones, and are commonly confined to the transpression zones. The bright pixels in the Nubian sandstone background can be attributed to the abundant detrital clay minerals.



Hydrothermal alteration zones also appear as bright pixels on the band ratios images of Sentinel-2 (Figure 9A–D). Band ratio 11/4 image shows gossan zones associated with tectonized ophiolites and island arc metavolcanic rocks (Figure 9A). Ferric oxides detected by band ratio 12/11 are mostly associated with the granitic rocks (Figure 9B). Ferrous silicates (biotite, chlorite, and amphibole) mapped by band ratio 12/11 are distinguished in island arc metavolcanic and metavolcaniclastic rocks and highly tectonized ophiolites (Figure 9C). Band ratio 11/12 enhances highly carbonated and deformed ophiolitic rocks in the ductile deformation zone, which are associated with highly tectonized ophiolites, metasediments and schists and island arc metavolcanic and metavolcaniclastic rocks. The results of alteration mapping derived from ASTER and Sentinel-2 datasets match and show the altered zones in both ductile and brittle deformation zones. Gossan, the chlorite/epidote/calcite mineral group, ferrous silicates and hydroxyl alteration zones are mapped in ductile (transpression) deformation zones, whereas ferric oxides are identified in the brittle (transtension) deformation zones.

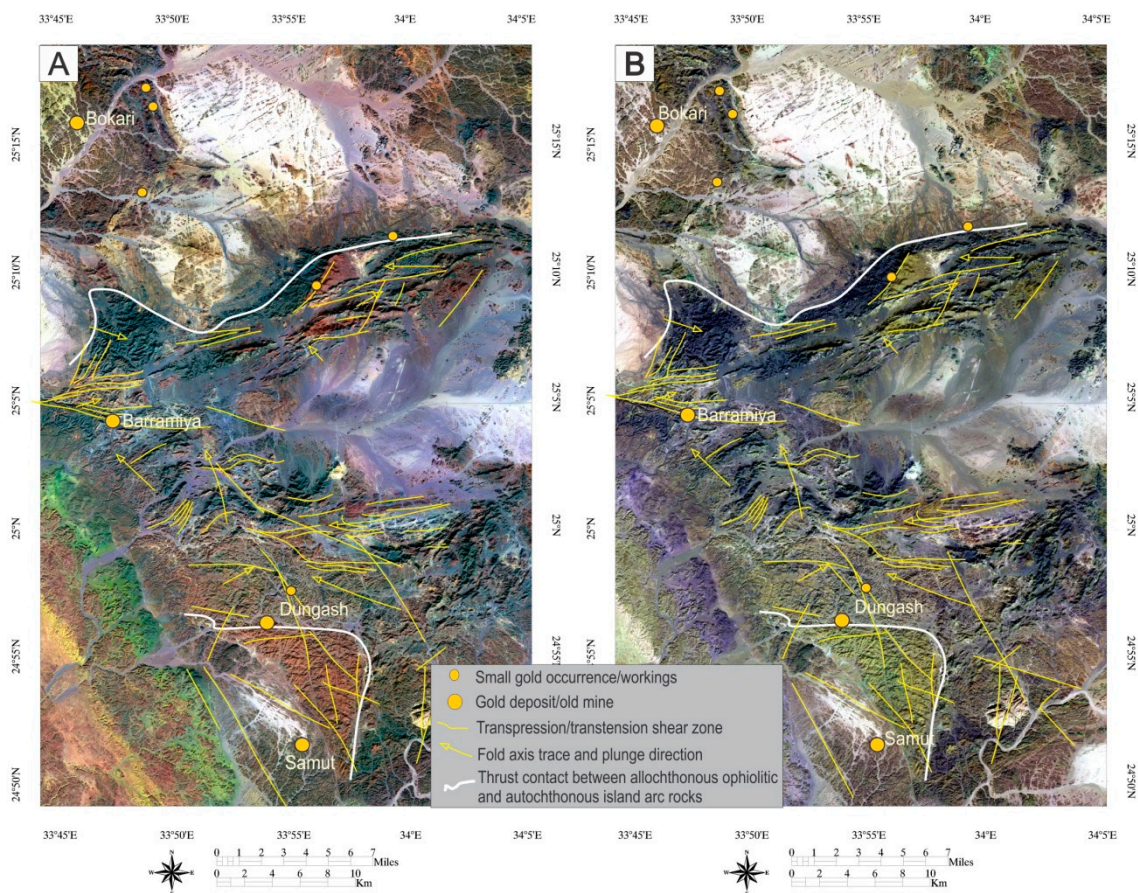


**Figure 7.** False-color composite, Sentinel-2 band combination images for the study area: (A) (R: Band 11, G: Band 8, B: Band 2), and (B) (R: Band 11, G: Band 12, B: Band 7) used to map  $\text{Fe}_2\text{O}_3/\text{MgO}$  and  $\text{Al}_2\text{O}_3$ -rich rocks, respectively. These images helped in differentiating the mafic and ultramafic ophiolitic from felsic rocks.



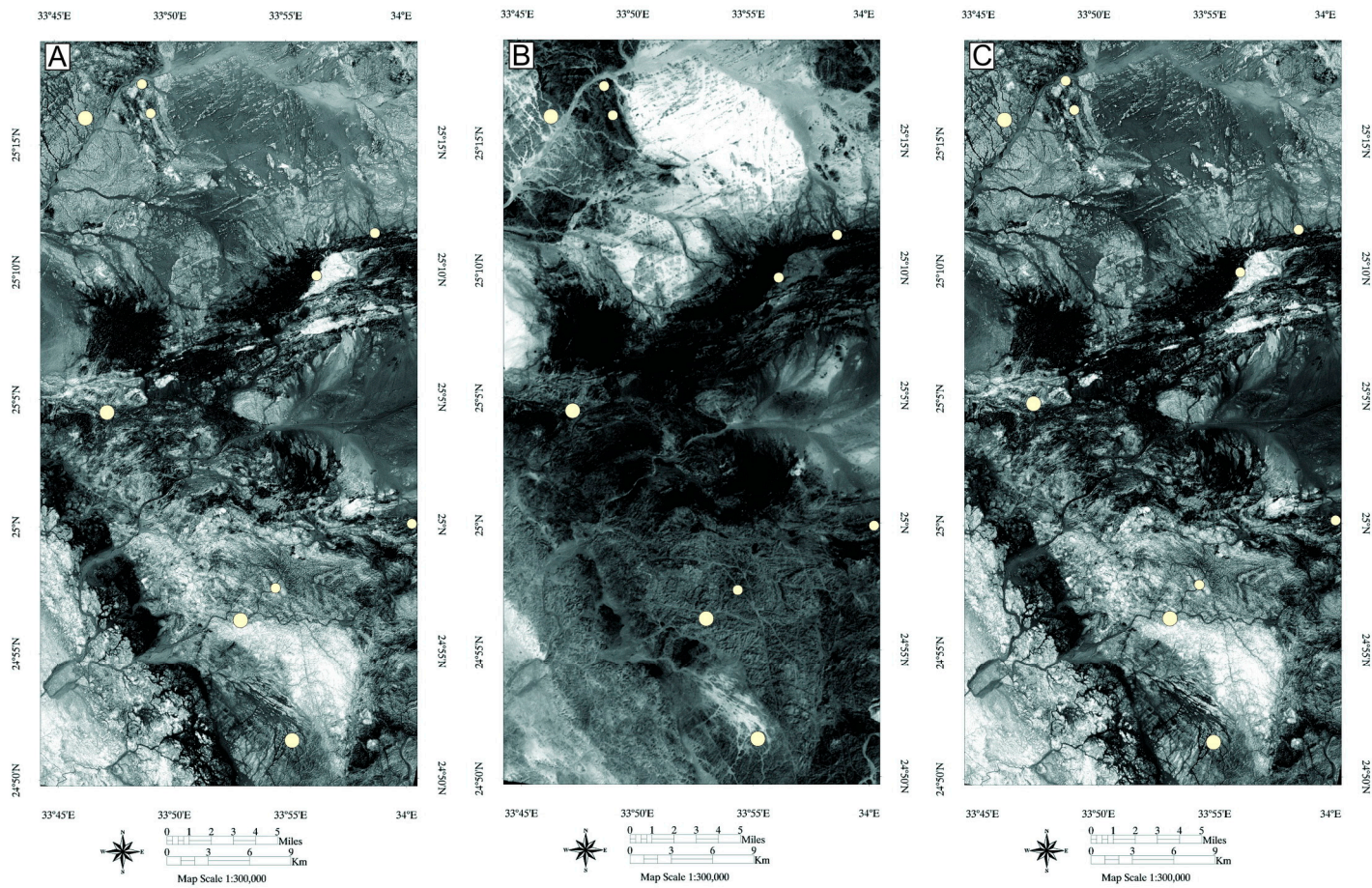


**Figure 8.** ASTER band ratio indices used to detect the hydrothermal alteration zones in the study area: (A) Band4/band2 image for mapping gossan zones, (B) Band4/band3 image for mapping ferric oxide-rich rocks, and (C) Band7+band9/band8 image for mapping chlorite/epidote/clacite-rich rocks. White circles are locations of gold deposits/occurrences.



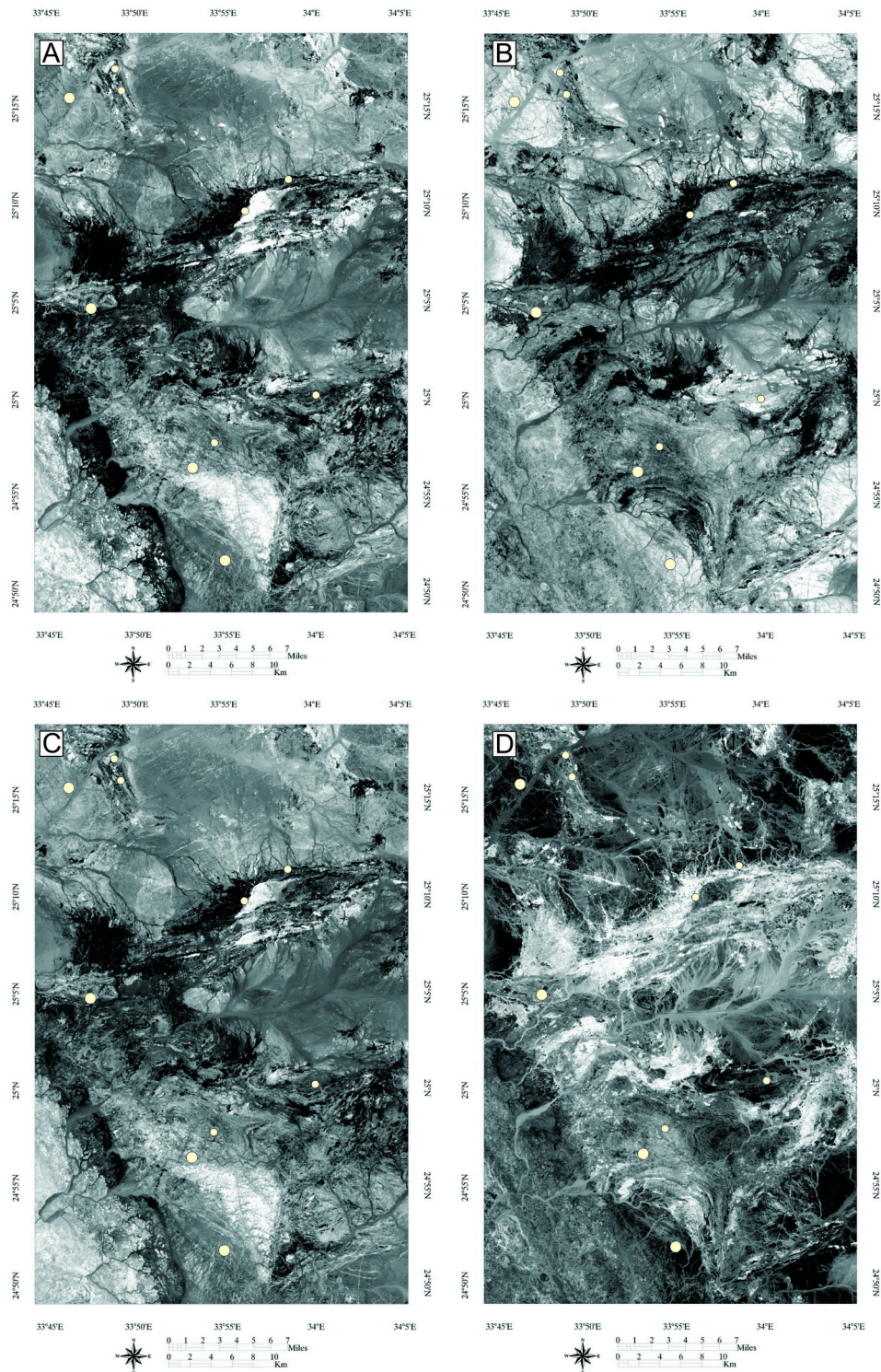


**Figure 9.** Band ratios of Sentinel-2 data used to map hydrothermal alteration zones in the study area: (A) band11/band4 image (for gossan mapping), (B) band11/band8a image (for ferric oxide-rich rocks), (C) band12/band11 image (for ferrous silicate-rich rocks), and (D) band11/band12 image (for hydroxyl alteration mapping).

## 4.2. Fieldwork Data Analysis

### 4.2.1. Structural Evolution of the Barramiya–Mueilha Area

Superimposed structural elements in the Barramiya–Mueilha area (Figure 10) are considered as manifestations of three phases of ductile deformations (D1, D2, D3). Extensional structures, e.g., fault/fracture zones and dike swarms cutting most of the ductile structures in different directions are signs of late brittle deformation (D4), most likely related to terrane cooling and exhumation during the orogen collapse [44,70–77].

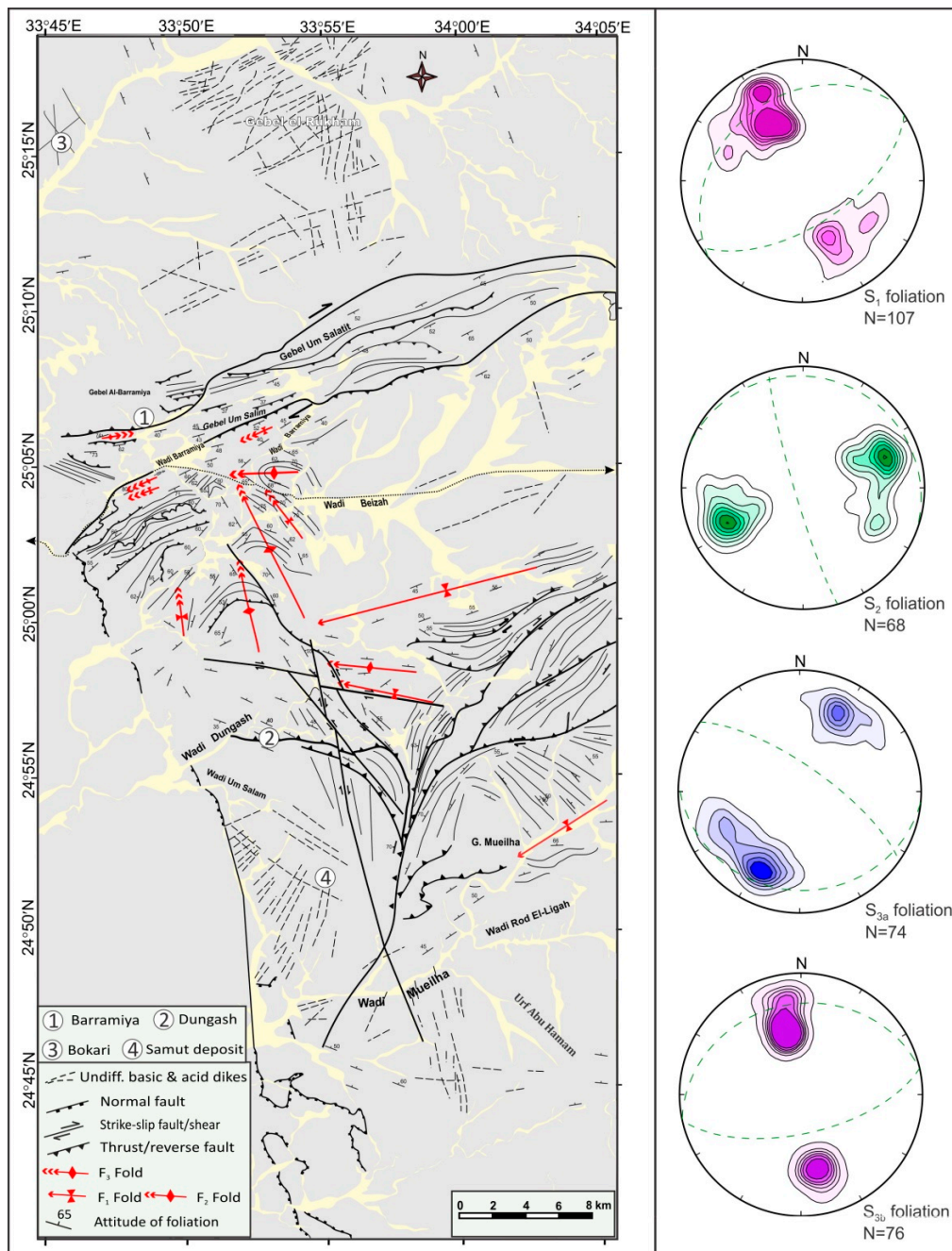


**Figure 10.** Simplified structural map of the Barramiya–Mueilha sector compiled from field measurements and satellite data interpretations. Several occurrences of gold–quartz veins are located in the area, but only significant gold occurrences/deposits are shown in the key. Insets are lower hemisphere stereographic projection for poles of the different generations of foliations.



#### 4.2.2. NNW–SSE Shortening and Southward Tectonic Transport

This event is characterized by stacking and imbrication of large ophiolitic nappes and best exemplified by  $S_1$  foliation (Figure 11A). Serpentinite in Barramiya and Dungash areas occurs as steeply dipping WNW- to NE-trending belts emplaced along thrust planes and stretched parallel to the penetrative foliation in the ophiolitic mélange.  $S_1$  is ENE-striking shear foliation developed around the thrust-bound ophiolites. ENE-trending mineral stretching lineation ( $L_1$ ) plunge gently (10–35°) mainly towards the ENE (Figure 11B). Schists, talc–magnesite rocks, listvenite and chromite pockets mark the tectonic contacts between the allochthonous serpentinite masses and the metasedimentary mélange matrix.

#### 4.2.3. NNE–SSW Shortening Structures

Steeply dipping NW–SE to WNW–ESE mineral foliation ( $S_2$ ), i.e., hornblende, epidote–chlorite, chlorite, tremolite, and graphite, are best developed in schistose rocks as well as sheared metagabbro, meta–agglomerate and metatuffs. The NW–SE Dungash–Beizah shear zone is marked by an intensification of  $S_2$  schistosity (Figure 11C) and locally by NE-dipping mylonitic foliation. Feldspar-rich and amphibole-rich bands define  $S_2$  foliation in the ophiolitic metagabbro. Mineral and stretching lineations are oriented close to fold axial plane.

#### 4.2.4. E–W Oblique Convergence

This phase of deformation was characterized by the main stress component ( $\sigma_1$ ) swinging between NE and SE, but the main shortening is considered E–W coinciding with the Arabian–Nubian Shield collision with the Nile Craton in the west. During D3a deformation, the Wadi Beizah imbricated thrust sheets of ophiolitic serpentinite and metagabbro were openly folded into a series of kilometre-scale NNW-trending asymmetric and plunging synclinal and anticlinal folds ( $F_{3a}$ ). These folds progressively open up westward, where fold hinges ( $L_{3a}$ ) plunge gently (~25°) to the NNW. Minor  $F_{3a}$  folds around the Dungash–Beizah shear zone display complex interference geometry with the development of both S and Z patterns commonly seen in scattered exposures (Figure 11E). Three types of NE- to ENE-striking cleavage ( $S_{3b}$ ) are recognized in the Barramiya–Mueilha area: Slaty, scaly and rhombohedral. Scaly and rhombohedral cleavage prevail in moderate to low strain sectors and in limbs of Z type and upright folds especially around Wadi Dungash and Mueilha (Figure 11F). A major NNE-trending shear zone occurs between metavolcanic and metavolcaniclastic rocks in the area between Wadi Dungash and Wadi Mueilha. This shear zone resembles a palm-tree structure, with the main segment striking NNE–SSW and dips steeply to WNW.

#### 4.2.5. Exhumation Tectonics

This phase is marked by sub vertical fractures including major brittle strike slip faults and micro-faults (Figure 11G,H) and dykes associated with intrusion of late to post tectonic granites. Structures assigned to this deformation stage comprise WNW–ESE dextral and NNW–SSE sinistral strike–slip faults that locally controlling felsic and mafic dikes in Gebel el–Rukham syn-tectonic granites as well as Um Salam and Urf Abu Hamam post tectonic granite.

#### 4.2.6. Gold Occurrences in the Barramiya–Mueilha Area

Several gold occurrences in the study area are mainly associated with high strain zones along the segmented thrust-bound ophiolitic belts in the central part of the map area. In the following we present some features of four important gold occurrences/deposits in the area, namely, Barramiya, Dungash, Bokari, and Samut (Figure 12).

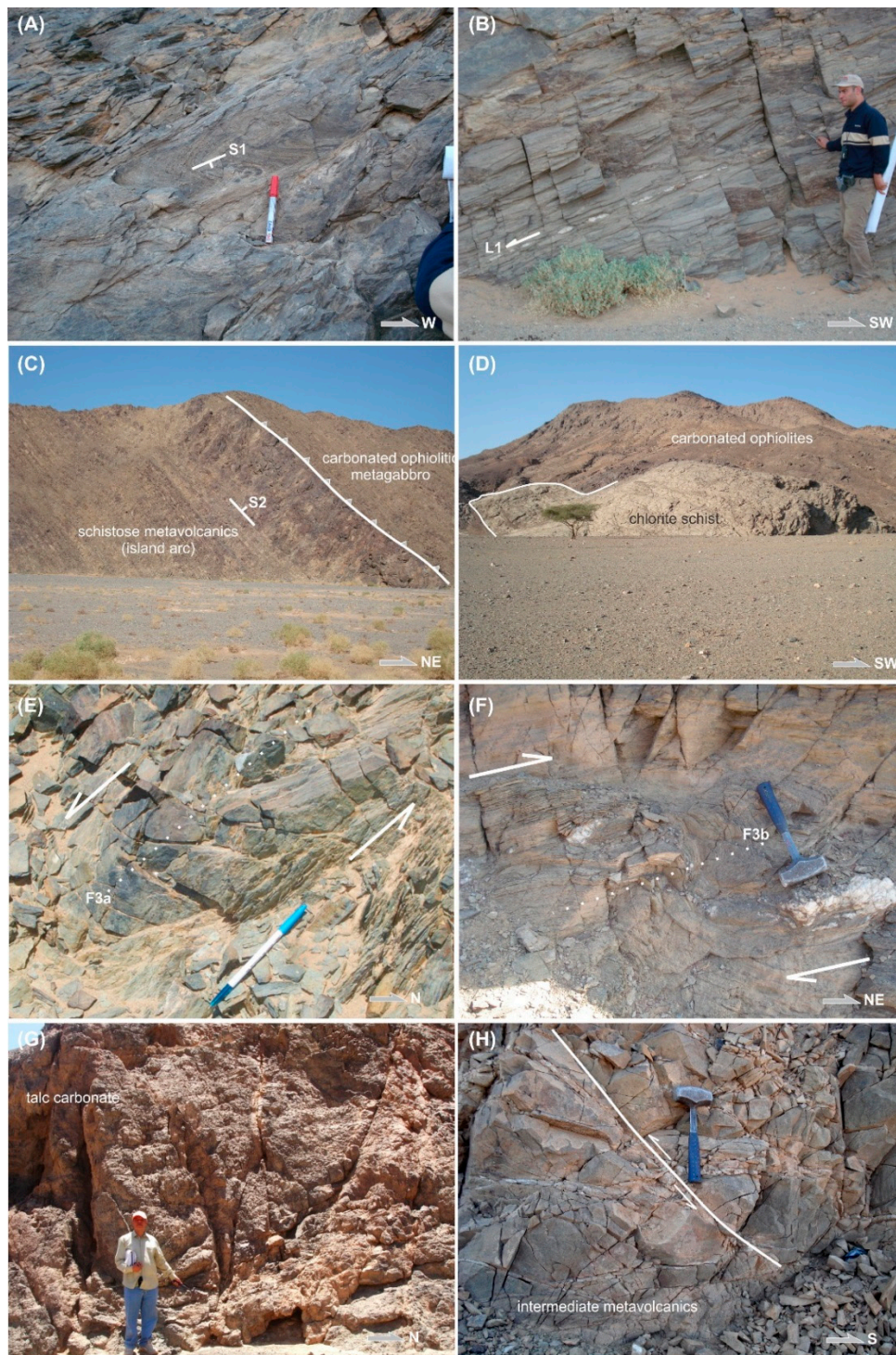


**Figure 11.** Field relationships of (A) NE-striking fold and  $S_1$  foliation preserved in the island arc metavolcanic rocks in north of Dungash mine, (B) Boudinage and shallowly-plunging stretching lineations ( $L_1$ ) in strongly foliated chlorite schist north of Dungash mine, (C) Steeply-dipping thrust contact between island arc and ophiolitic rocks and best preserved ENE-striking  $S_2$  foliation east of Dungash mine, (D) Carbonated ophiolitic serpentinite tectonically overlying chlorite schist and separated by a WNW-striking thrust fault north of the Barramiya mine, (E)  $F_{3a}$  fold with a sinistral asymmetry developed in metasedimentary rocks south of the Barramiya mine, (F)  $F_{3b}$  asymmetrical fold indicating a dextral shear sense and is associated with dilation-controlled quartz pods, (G) ~E–W fracture system in talc carbonate north of the Barramiya mine, (H) Dissecting joint/fracture sets with quartz-hosted ones displaced by later sinistral exposure-scale faults south of the Dungash mine.



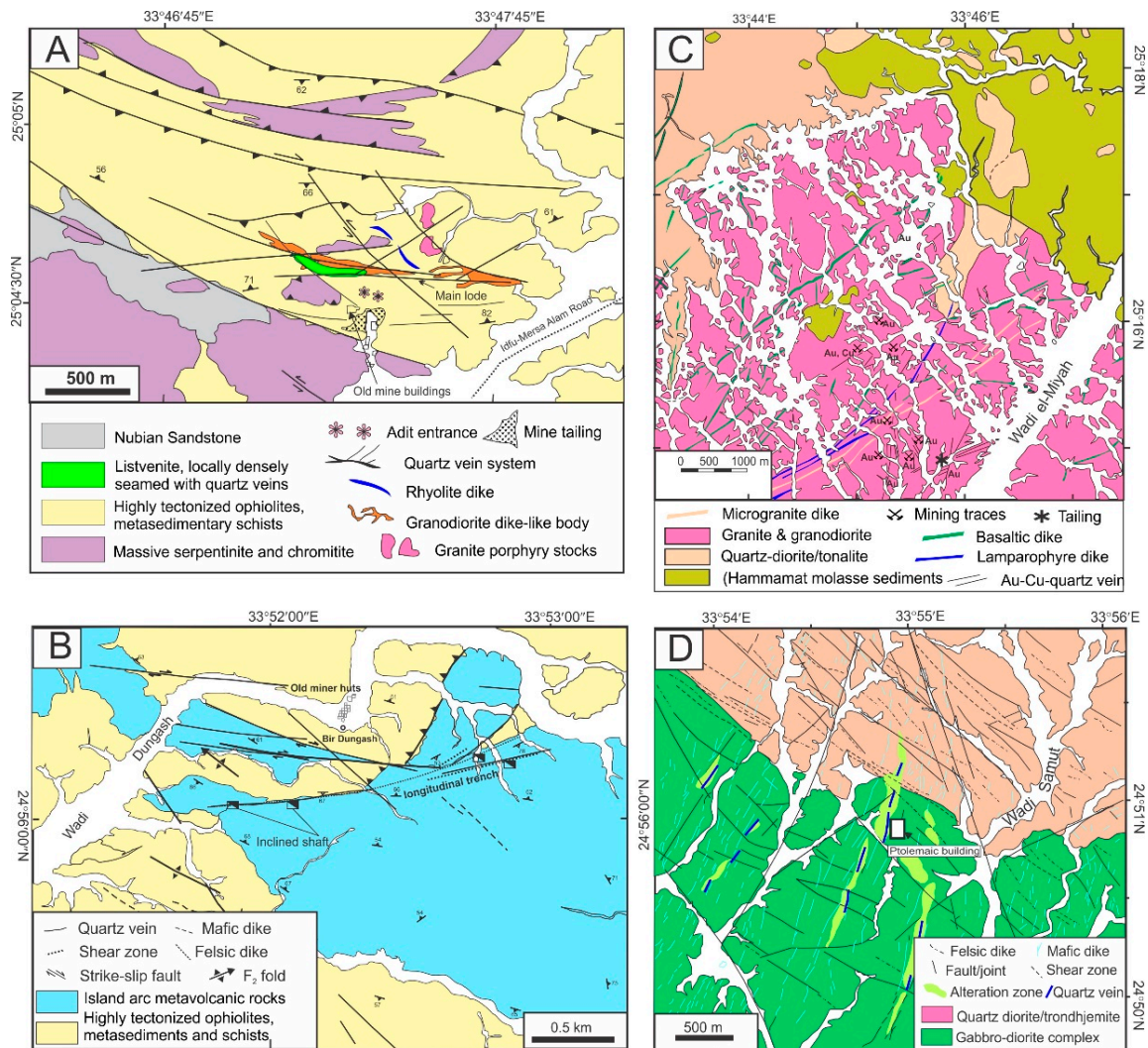


**Figure 12.** Detailed geological maps of the selected gold occurrences/deposits in the study area, (A) Barramiya deposit area, after [36], (B) Dungash deposit area, after [37], (C) Bokari deposit area, after [78], and (D) Samut gold deposit area, after [46].

### Barramiya Gold Deposit

The Barramiya gold deposit (Figure 12A) is expressed in auriferous quartz and quartz–carbonate veins cutting altered and carbonaceous ophiolitic mélangé serpentinite and metasiltstone (Figure 13A). The main ore body or the main lode extends for 900–1,100 m along the strike and exhibits common pinch and swell morphologies [79,80]. The internal structure of the mineralized veins comprises massive and laminated quartz veins with abundant slivers of pervasively carbonated wallrock. Zoheir and Lehmann [35] proposed a genetic relationship between gold mineralization and listvenite and listvenitized ophiolitic rocks in the Barramiya mine area (Figure 13A–D). Cr-chlorite and Cr-sericite are manifestations of K-metasomatism of the ophiolitic serpentinite, and reflect the crucial role played by a small granitic intrusion (exposed north of the ophiolitic belt) in formation of the Barramiya gold deposit. Fire assay analysis of the highly ferruginated/silicified listvenite samples gave high gold contents (up to 11 ppm) in several cases [81]. Gold-associated sulfides include arsenopyrite, pyrite and subordinate sphalerite, chalcopyrite, pyrrhotite, tetrahedrite, galena, and gersdorffite. Marcasite and covellite occur as supergene replacements of pyrite and chalcopyrite, respectively. Free gold and electrum blebs and scattered spikes are seen in the micro-fractured sulfides and recrystallized quartz veins.

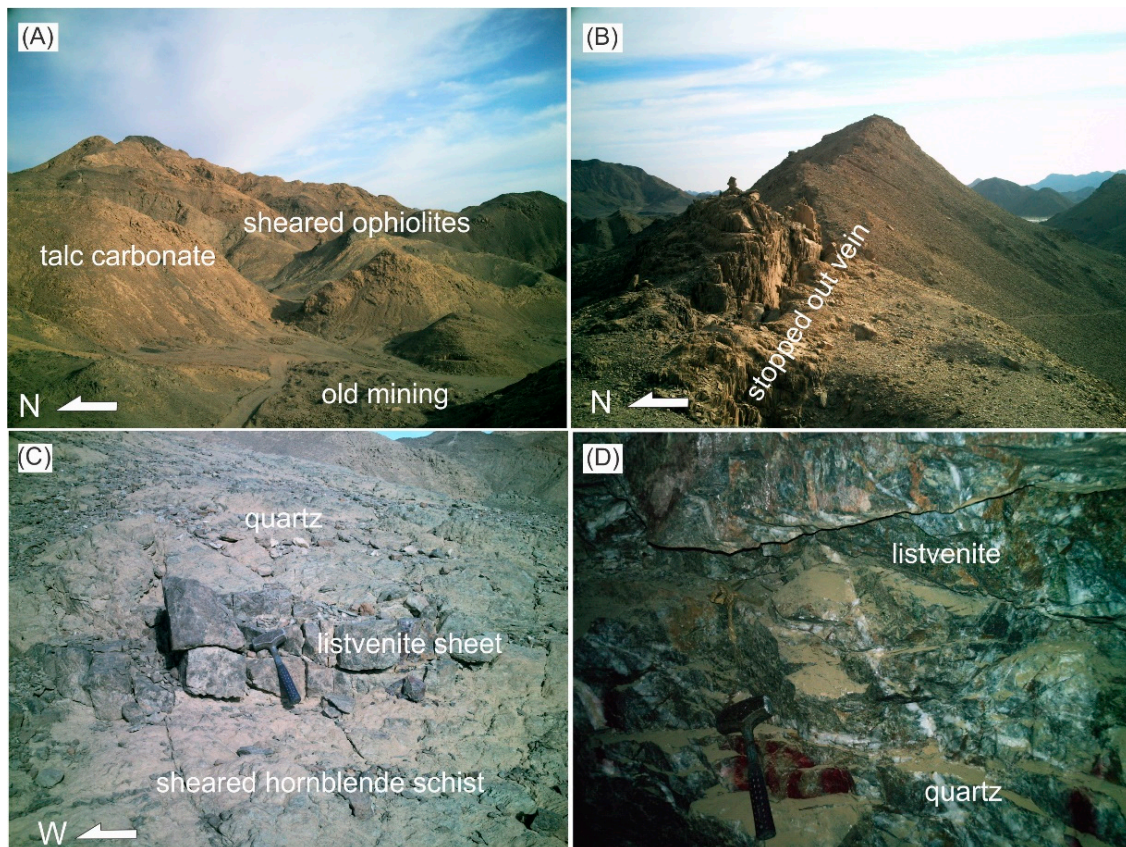


**Figure 13.** Field relationships at the Barramiya mine area and its surroundings, including: (A) Sheared ophiolitic serpentinite and talc carbonate exposures north of the Barramiya mine where scattered old mining activities are observed, (B) ~E–W trending quartz vein significantly worked out by old miners and still preserves the trend of the main lode of the Barramiya deposit, (C) Listvenite sheet embedded within shear hornblende and actinolite schist north of the Barramiya mine, and (D) Typical listvenite exposure in the underground mine levels dissected by milky quartz veins.

### Dungash Gold Deposit

The Dungash gold deposit is related to ~E-trending dilation zones in variably sheared island arc metavolcanic and metavolcaniclastic rocks (Figure 12B). The vein morphology and structures suggesting gold–quartz vein formation synchronous with dextral transpression and flexural displacement of heterogeneously folded greenstone belts (Figure 14A). In the eastern part of the mine area, the main quartz vein occurs along an undulating shear zone between the schistose rocks and heterogeneously foliated trachyandesite and extends further E into andesite and plunges into SE and is associated with pervasive epidote–chlorite alteration (Figure 14B). The hydrothermal alteration assemblages related to the gold–quartz veins include sulfide, carbonate, epidote, chlorite, iron oxides, and sericite (Figure 14B–D) replacing feldspar and ferromagnesian minerals in rhyodacitic metavolcanic rocks in the western mine [82,83]. The mineralized quartz veins are sulfide-rich and are associated with mylonite zones along reverse faults (Figure 14E). In places, quartz veins are bound by carbonate pockets with well crystalline calcite apparently late than ankerite disseminations (Figure 14F). Arsenopyrite, As-pyrite, gersdorffite and less abundant pyrrhotite are replaced in part by a late-paragenetic sulfide assemblage comprising tetrahedrite, chalcopyrite, sphalerite, galena, and free gold.



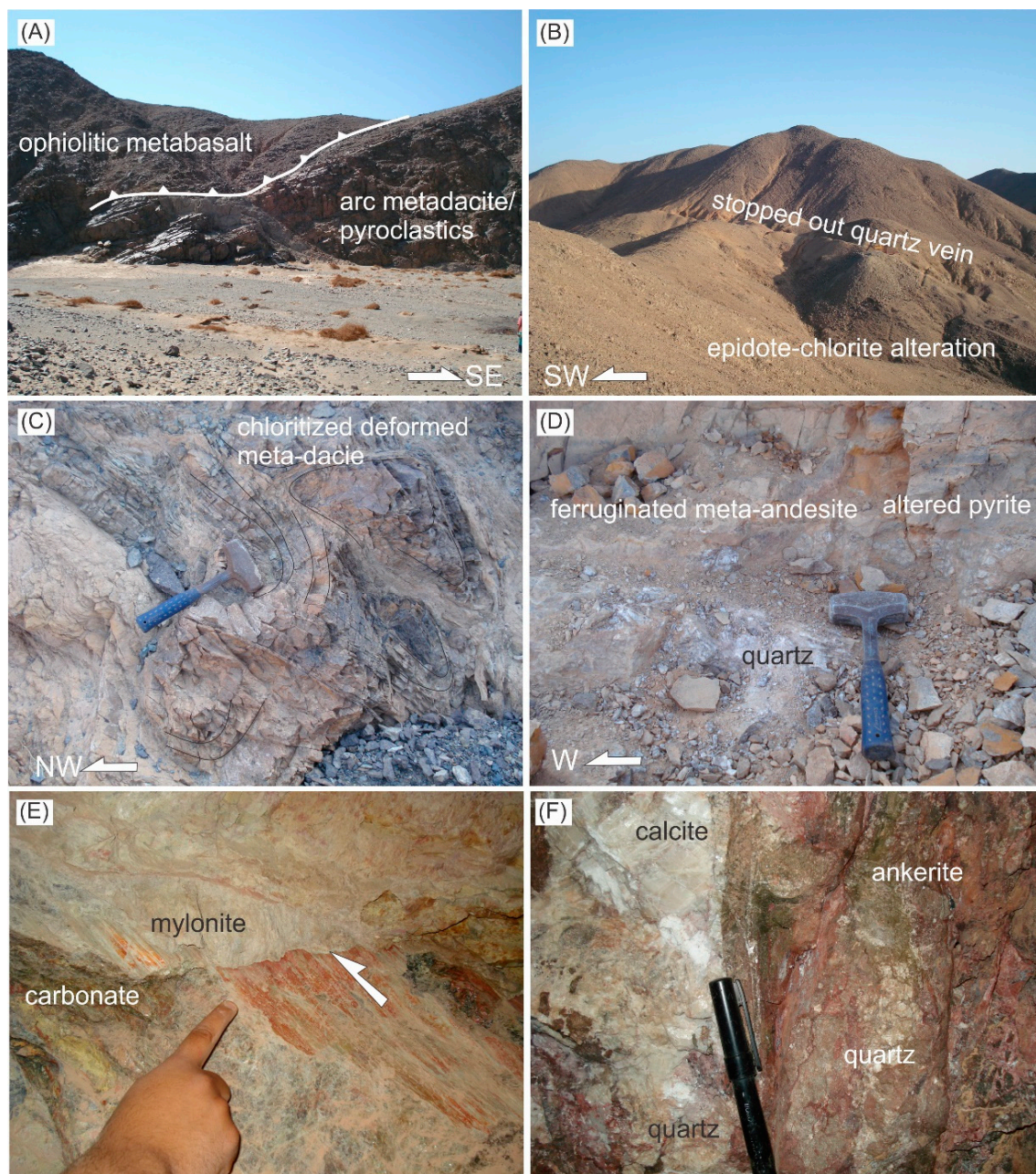


**Figure 14.** Field relationships at the Dungash mine area and its surroundings, including: (A) Ophiolitic metabasalt tectonically overlies the island arc metavolcanic rocks north of the Dungash mine, (B) Traces of ~ E–W trending gold-bearing quartz vein (main lode) and associated epidote–chlorite alteration in Dungash mine, (C) Deformed felsic metavolcanic rocks embedded in pervasively carbonated and chloritized material, (D) Disseminated altered sulfides and iron oxides (ferrugination) in the vicinity of mineralized quartz–ankerite vein, (E) Carbonate alteration along slicken planes on a reverse fault and associated mylonite zone in the underground levels of Dungash mine, (F) Ankerite and calcite associated with quartz veins.

#### Bokari Gold Occurrence

The Bokari gold occurrence (also known as Bakriya occurrence; 25°15'30"N, 33°45'15"E) occurs along Wadi Bokari to the north of Wadi el-Miyah, some 20 km north of the Barramiya mine. Gold mineralization is related mostly to milky quartz veins along fault and fracture zones cutting across variably deformed quartz–diorite to granodiorite intrusion and country gabbro–diorite complex



(Figure 12C). Shearing in the area is dominantly brittle, with alteration zones and quartz veins are generally associated with mylonite zones (commonly <0.5 m wide; Figure 15A). Scattered mine ruins of quartz vein and Wadi alluvium workings dating back to the Pharaohs and Early Arab times, but also from the Roman-Byzantine era, have been reported [78]. In places, sericite alteration is pervasive and kaolinite associates basic dikes and quartz veins (Figure 15B). The main feature in the Bokari mine is that gold-bearing quartz veins and ruins of old mining are confined to zones where the host granodioritic rocks are intensely brecciated (Figure 15C). The main quartz veins trend consistently to N (Figure 15D).

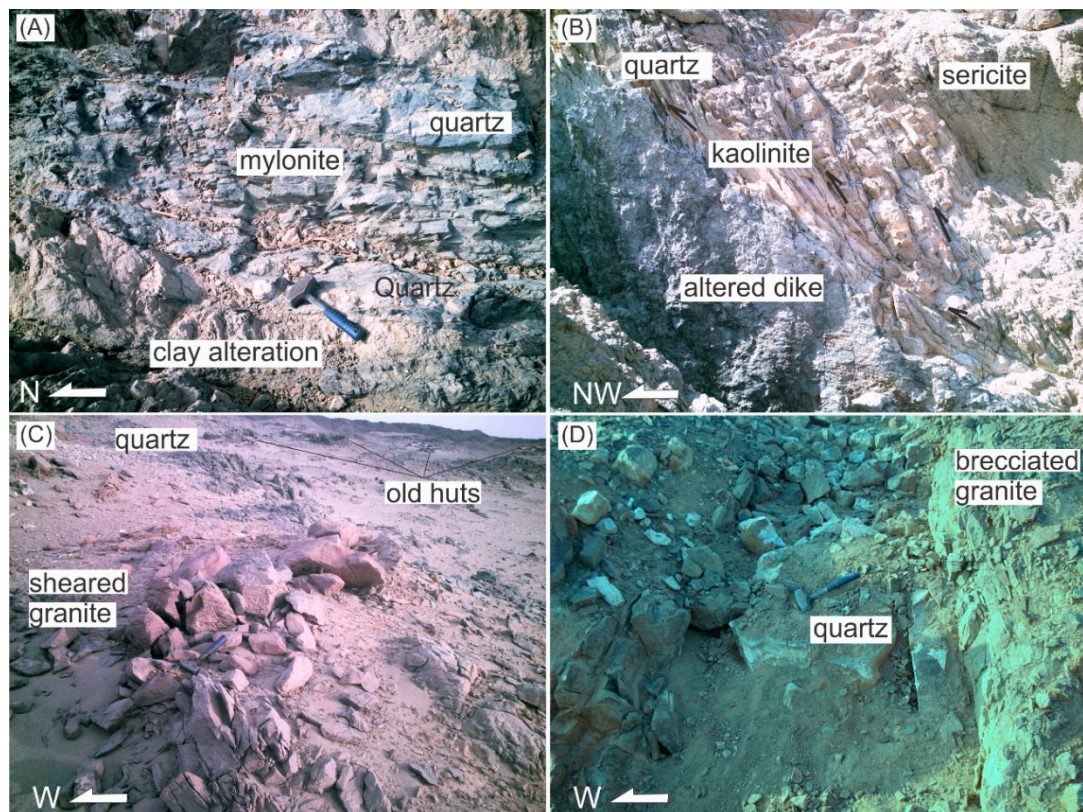


**Figure 15.** Field relationships of the mineralized quartz veins in the Bokari mine area: (A) Mylonite zone and associated quartz vein on one side and clay mineral alteration on the other side, (B) Kaolinite and quartz veins bordered by sericitized granodiorite and altered basic dike at the Bokari mine, (C) Scattered quartz vein segments and pockets in brecciated granodiorite near old miner huts at the Bokari mine area, (D) Thick (~1 m-thick) quartz vein trending ~N–S and is mined out selectively in areas where hydrothermal alteration selvages are abundant, whereas zones lacking the altered wallrock are not mined (barren?).

### Samut Gold Deposit

The Samut gold deposit is related to milky and reddish quartz that cut through terranes of gabbro–diorite complex adjacent to its lithological contact with a quartz diorite/trondhjemite intrusion (Figure 12D). The main quartz vein (~2 m-thick) extends for more than 400 m along the ~ NNE–SSW strike direction. Other minor quartz veins are parallel to ~N or NNE-trending mafic dikes within and external of the Samut mine area [84]. The internal structures of the auriferous lodes comprise laminated quartz–chalcedony bands and vuggy comb, well-crystalline quartz. Hematite, sericite, kaolinite, ankerite, and calcite are common alteration phases in the marginal zones of quartz veins (Figure 16A–C). Quartz–carbonate veins (Figure 16D) are reported as the high grade ore bodies in the mine area. Gold-associated sulfides include abundant pyrite and minor sphalerite, chalcopyrite, galena, arsenopyrite, and marcasite scattered in the auriferous quartz veins





**Figure 16.** Field relationships of the orebodies at the Samut mine area showing: (A), (B), (C) Mineralized quartz veins at the Samut mine area, commonly associated with sericite, kaolinite, and sulfide alteration. Notice that the alteration zones are of limited thickness (commonly <0.5 m-wide), (D) Brecciated quartz vein exposed in the underground mine levels with abundant wall rock material and disseminated pyrite and chalcopyrite, locally altered into malachite and limonite, respectively.

## 5. Discussion

Orogenic gold deposits are commonly associated with large-scale, terrane-bounding fault systems and deformation belts, commonly described as orogenic belts [85,86]. Transpression and transtension tectonics occur where deformation is supplemented by a significant volume change, i.e., in oblique subduction margins in the arc, forearc, and back-arc environments [87–90]. These zones can also develop in restraining and releasing bends of major transform and dislocation zones, particularly throughout the early stages of continental rifting or during the late orogenic extension [87–95]. In such high strain zones, mineral deposits other than orogenic gold include different associations of elements such as Sn, W, U, Th, Mo, Cu, Au, Pb, Zn, Ag, Nb, Ta, Be, Sc, Li, Y, Zr, Sb, F, Bi, As, Hg, Fe, Ga, REEs [96–100]. Space-borne multispectral and radar imagery data provide great information for detailed structural, lithological, and alteration mapping to prospect a variety of these mineral resources in regional transpression and transtension zones [90].

Multi-sensor satellite imagery data, including Sentinel-1, PALSAR, ASTER, and Sentinel-2 are integrated here with field data are found efficient in mapping the different geological structures and alteration zones in the Barramiya–Mueilha sector of the Nubian Shield in Egypt. The belt is characterized by highly sheared ophiolite blocks, oppositely dipping, ENE–WSW thrusts, and less abundant NW-trending fault/shear zones [78,101,102]. Ductile shear zones developed in the highly sheared, refolded ophiolitic and island arc rocks in the central part of the study area host several occurrences of orogenic gold in the ophiolitic mélange (e.g., the Barramiya deposit) or along the decollement boundaries between ophiolites and island arc domains (e.g., the Dungash deposit) (Figure 17).



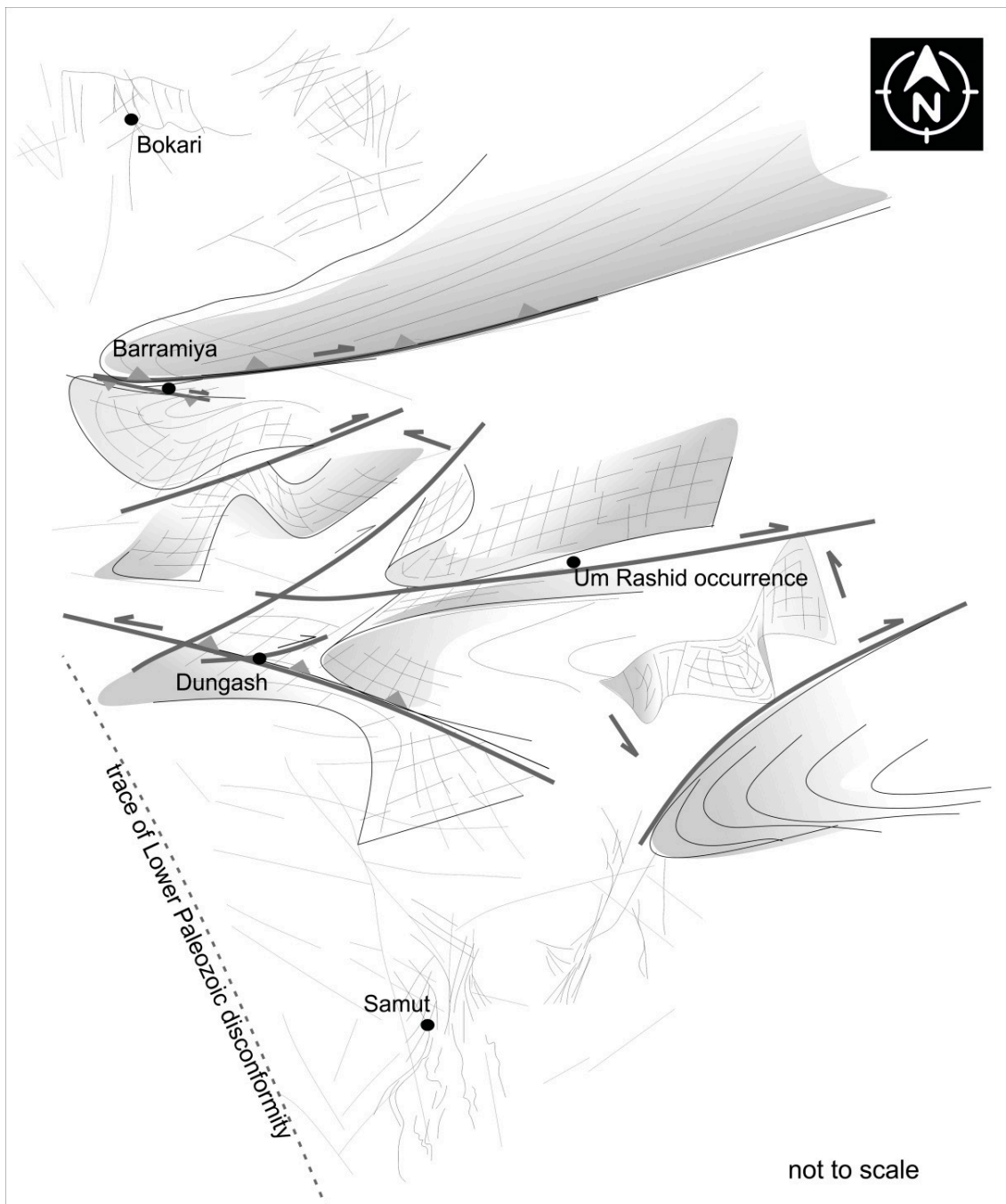


**Figure 17.** Sketch drawing explains the fold interference and location of transpression and transtension structures in the Barramiya–Mueilha sector. Notice that the Barramiya and Dungash deposits (and many small occurrences from which only Um Rashid is shown) are confined to transpression zones within the highly strained rocks or at their margins. The Samut and Bokari gold deposits, in contrast, are hosted by transtension zones within the granitoid/gabbroid terranes.

Gold–quartz veins in these deposits show characteristically abundant plastic deformation textures, consistently in ~E–W direction conformable with the variably carbonated, talcous ophiolitic belts of serpentinite, chromitites, and listvenite. On the other hand, gold occurrences in the northern and southern parts of the study area are restricted to zones brittle (transtension) deformation in gabbro–diorite complex where cut by quartz–diorite/trondhjemite and alkali feldspar granite intrusions.

Gold–quartz veins in these occurrences are controlled mainly by rather narrow NNE–SSW or N–S fault/fracture zones (Figure 17) with abundant brecciation and mylonitization textures.

The FPCS2 image-maps (Figures 2 and 3) of Sentinel-1 and PALSAR data derived from cross-polarized backscatter ratio images detect structural elements related to transtension and transpression zones in the study area. The transtension zone is identified based on lack of intensity in foliation or any development of shear cleavage. However, intense foliation and shear cleavage are detected in transpression zones. PALSAR data hold more proficiency to map the geological structures covered by desert sand, hence, detailed textural variability and tonal variation are mapped for intensely sheared ophiolitic nappes and island arc metavolcanic and metavolcaniclastic rocks in FPCS2 PALSAR image-maps. The RGB color composite of the PC1, PC2, and PC3 of ASTER (VNIR + SWIR) and Sentinel-2 bands (Figures 4A and 5A) map variety of the lithological units contain discernible spectral features in the study area, while the lithologies with identical spectral characteristics exhibit similar hue in the image-maps. RGB color composite image of PC4, PC5, and PC6 of ASTER VNIR + SWIR bands highlights alteration mineral assemblages associated with the highly tectonized ophiolites and schists, island arc metavolcanic rocks, alkali-feldspar granite and granitoids background, ophiolitic serpentinite, chromitite and ultramafic rocks and metagabbro–diorite complex (Figure 4B). The RGB color composite image-map derived from PC6, PC5, and PC4 of Sentinel-2 datasets (Figure 5B) is capable of mapping hydrous minerals and Fe-oxides/hydroxides associated with the highly tectonized ophiolites, metasediments and schists, post-orogenic alkali-feldspar granite, syn-orogenic granitoids and island arc metavolcanic and metavolcaniclastic rocks in both ductile and brittle zones. Compressional structures in the central part of the study area accommodate hydrothermal extensive zones. Hydroxyl minerals and iron oxide/hydroxide zones are specifically mapped and discriminated by ASTER, despite the fact that they are mixed with each other in the Sentinel-2 results. Iron oxide/hydroxide minerals and mafic lithologies (metagabbro–diorite complex) are strongly detected by Sentinel-2 bands.

Fe<sub>2</sub>O<sub>3</sub>/MgO-rich rocks (ophiolitic serpentinite and metagabbro–diorite complex) and Al<sub>2</sub>O<sub>3</sub>-rich rocks (alkali-feldspar granite and granitoids) are easily mapped by ASTER and Sentinel-2 data band combination (Figures 6 and 7). A series of band ratio indices images for ASTER and Sentinel-2 data enabled the delineation of the hydrothermal alteration zones, which most associate with the major shear ductile zones. However, the resultant image-maps of alteration minerals derived from ASTER and Sentinel-2 datasets are almost identical. The alteration minerals zones are found in both ductile and brittle deformation zones. Gossan, the chlorite/epidote/calcite mineral group, ferrous silicates and hydroxyl alteration zones are mostly mapped in the transpression zones, whereas ferric oxides are typically detected in the transtension zones. Fieldwork and GPS surveying verified the scatter of alteration minerals and zones and their association with geological structures in the study area.

## 6. Conclusions

The space-borne radar (Sentinel-1 and PALSAR) and multispectral (ASTER and Sentinel-2) imagery data were coupled with comprehensive field observations and structural measurements to unravel the structural control of gold occurrences and alteration zones in the Barramiya–Mueilha sector. Gold mineralization in particular locations is constrained by the combined effect of transpression and transtension tectonics throughout the deformational history of the area. Application of the FPCS technique to the backscatter ratio images of Sentinel-1 and PALSAR datasets promoted detailed mapping of the major lineaments, curvilinear structures, and intersections associated with transpression and transtension zones in the study area. The results revealed that foliation and shear cleavage superimposition and shear-controlled gossan and carbonate alteration can be used as a criterion to distinguish the transpression zones. The transtension zones, on the other hand, are characterized by heterogeneous strain and irregular haloes of ferrugination and hydroxyl alteration. The PCA of the ASTER and Sentinel-2 bands, band combination and band ratioing techniques promoted the spectral discrimination between the lithological units and alteration zones. The combination of the remote



sensing results and field data designates that gold-bearing quartz veins are restricted to high strain (transpression) zones in the ophiolite-island arc belts, particularly where carbonated or listvenized. Gold occurrences in granitoid–gabbroid domains are controlled by fault and brittle shear zones assigned to as antithetic sets in a rejuvenated transpression–transtension regime operated intermittently from the orogenic collision to orogen collapse. The radar and multispectral satellite data abetted a better understanding of the structural framework and unraveled settings of the scattered gold occurrences in the study area. An outlook study will need to consider the GIS-based morphometric analysis of the different geomorphometric features (i.e., regional ductile and brittle structures) based on high spatial resolution DEM data.

**Author Contributions:** Conceptualization & Research Initiation, B.Z.; Methodology, B.Z., M.A., A.B.P. and A.A.; Remote Sensing Data Acquisition and Analysis, B.Z. and A.B.P.; Field Investigation & Validation, B.Z., M.A. and A.A.; Writing-Original Draft Preparation, B.Z., M.A., A.B.P. and A.A.; Writing-Review & Editing, B.Z., A.B.P., M.A., and A.A. Publication fees are waived by Remote Sensing as A.B.P. and B.Z. are guest editors.

**Funding:** This research received no external funding

**Acknowledgments:** Basem Zoheir thanks the Alexander von Humboldt foundation for making this work possible. A.B. Pour is indebted to the Korea Polar Research Institute (KOPRI) for assigned time, providing the computer and software facilities.

**Conflicts of Interest:** The authors declare no conflict of interest.

## References

1. Zoheir, B.A.; Emam, A. Field and ASTER imagery data for the setting of gold mineralization in Western Allaqi-Heiani belt, Egypt: A case study from the Haimur. *J. Afr. Earth Sci.* **2014**, *66–67*, 22–34. [[CrossRef](#)]
2. Zoheir, B.A.; Emam, A.; El-Amawy, M.; Abu-Alam, T. Auriferous shear zones in the central Allaqi-Heiani belt: Orogenic gold in post-accretionary structures, SE Egypt. *J. Afr. Earth Sci.* **2018**, *146*, 118–131. [[CrossRef](#)]
3. Testa, F.J.; Villanueva, C.; Cooke, D.R.; Zhang, L. Lithological and hydrothermal alteration mapping of epithermal, porphyry and tourmaline breccia districts in the Argentine Andes using ASTER imagery. *Remote Sens.* **2018**, *10*, 203. [[CrossRef](#)]
4. Pour, A.B.; Park, T.S.; Park, Y.; Hong, J.K.; Zoheir, B.; Pradhan, B.; Ayoobi, I.; Hashim, M. Application of multi-sensor satellite data for exploration of Zn-Pb sulfide mineralization in the Franklinian Basin, North Greenland. *Remote Sens.* **2018**, *10*, 1186. [[CrossRef](#)]
5. Noori, L.; Pour, B.A.; Askari, G.; Taghipour, N.; Pradhan, B.; Lee, C.-W.; Honarmand, M. Comparison of Different Algorithms to Map Hydrothermal Alteration Zones Using ASTER Remote Sensing Data for Polymetallic Vein-Type Ore Exploration: Toroud–Chahshirin Magmatic Belt (TCMB), North Iran. *Remote Sens.* **2019**, *11*, 495. [[CrossRef](#)]
6. Sheikhrasimi, A.; Pour, B.A.; Pradhan, B.; Zoheir, B. Mapping hydrothermal alteration zones and lineaments associated with orogenic gold mineralization using ASTER remote sensing data: A case study from the Sanandaj-Sirjan Zone, Iran. *Adv. Space Res.* **2019**, *63*, 3315–3332. [[CrossRef](#)]
7. Woodhouse, I.H. *Introduction to Microwave Remote Sensing*; CRC Press: Boca Raton, FL, USA; Taylor & Francis Group: Boca Raton, FL, USA, 2006.
8. Abdelsalam, M.G.; Robinson, C.; El-Baz, F.; Stern, R. Application of orbital imaging radar for geologic studies in arid regions: The Saharan Testimony. *Photogramm. Eng. Remote Sens.* **2000**, *66*, 717–726.
9. Kusky, T.M.; Ramadan, T.M. Structural controls on Neoproterozoic mineralization in the South Eastern Desert, Egypt: An integrated field, Landsat TM, and SIR-C/X SAR approach. *J. Afr. Earth Sci.* **2002**, *35*, 107–121. [[CrossRef](#)]
10. Pour, A.B.; Hashim, M. Structural geology mapping using PALSAR data in the Bau gold mining district, Sarawak, Malaysia. *Adv. Space Res.* **2014**, *54*, 644–654. [[CrossRef](#)]
11. Pour, A.B.; Park, Y.; Crispini, L.; Läufer, A.; Kuk Hong, J.; Park, T.-Y.S.; Zoheir, B.; Pradhan, B.; Muslim, A.M.; Hossain, M.S.; et al. Mapping Listvenite Occurrences in the Damage Zones of Northern Victoria Land, Antarctica Using ASTER Satellite Remote Sensing Data. *Remote Sens.* **2019**, *11*, 1408. [[CrossRef](#)]

12. Pour, A.B.; Hashim, M.; Park, Y.; Hong, J.K. Mapping alteration mineral zones and lithological units in Antarctic regions using spectral bands of ASTER remote sensing data. *Geocarto Int.* **2018**, *33*, 1281–1306. [[CrossRef](#)]
13. Pour, A.B.; Hashim, M.; Hong, J.K.; Park, Y. Lithological and alteration mineral mapping in poorly exposed lithologies using Landsat-8 and ASTER satellite data: North-eastern Graham Land, Antarctic Peninsula. *Ore Geol. Rev.* **2019**, *108*, 112–133. [[CrossRef](#)]
14. Pour, B.A.; Hashim, M. Structural mapping using PALSAR data in the Central Gold Belt, Peninsular Malaysia. *Ore Geol. Rev.* **2015**, *64*, 13–22. [[CrossRef](#)]
15. Pour, A.B.; Hashim, M.; Makoundi, C.; Zaw, K. Structural Mapping of the Bentong-Raub Suture Zone Using PALSAR Remote Sensing Data, Peninsular Malaysia: Implications for Sediment-hosted/Orogenic Gold Mineral Systems Exploration. *Resour. Geol.* **2016**, *66*, 368–385. [[CrossRef](#)]
16. Adiri, Z.; Harti, A.; Jellouli, A.; Lhissou, R.; Maacha, L.; Azmi, M.; Zouhair, M.; Bachaoui, M. Comparison of Landsat-8, ASTER and Sentinel 1 satellite remote sensing data in automatic lineaments extraction: A case study of Sidi Flah-Bouskour inlier, Moroccan Anti Atlas. *Adv. Space Res.* **2017**, *60*, 2355–2367. [[CrossRef](#)]
17. Hamimi, Z.; El-Fakharani, A.; Emam, A.; Barreiro, J.G.; Abdelrahman, E.; Abo-Soliman, M.Y. Reappraisal of the kinematic history of Nugrus shear zone using PALSAR and microstructural data: Implications for the tectonic evolution of the Eastern Desert tectonic terrane, northern Nubian Shield. *Arab. J. Geosci.* **2018**, *11*, 494. [[CrossRef](#)]
18. Javhar, A.; Chen, X.; Bao, A.; Jamshed, A.; Yunus, M.; Jovid, A.; Latipa, T. Comparison of Multi-Resolution Optical Landsat-8, Sentinel-2 and Radar Sentinel-1 Data for Automatic Lineament Extraction: A Case Study of Alichur Area, SE Pamir. *Remote Sens.* **2019**, *11*, 778. [[CrossRef](#)]
19. Hunt, G.R.; Ashley, P. Spectra of altered rocks in the visible and near infrared. *Econ. Geol.* **1979**, *74*, 1613–1629. [[CrossRef](#)]
20. Clark, R.N.; King, T.V.V.; Klejwa, M. and Swayze, G.A. High spectral resolution reflectance spectroscopy of minerals. *J. Geophys. Res.* **1990**, *95*, 12653–12680. [[CrossRef](#)]
21. Huntington, J.F. The role of remote sensing in finding hydrothermal mineral deposits on Earth. *Evol. Hydrother. Ecosyst. Earth Mars* **1996**, *21*, 214–234.
22. Kruse, F.A.; Perry, S.L. Mineral mapping using simulated Worldview-3 short-wave-infrared imagery. *Remote Sens.* **2013**, *5*, 2688–2703. [[CrossRef](#)]
23. Askari, G.; Pour, A.B.; Pradhan, B.; Sarfi, M.; Nazemnejad, F. Band Ratios Matrix Transformation (BRMT): A Sedimentary Lithology Mapping Approach Using ASTER Satellite Sensor. *Sensors* **2018**, *18*, 3213. [[CrossRef](#)]
24. Haselwimmer, C.E.; Riley, T.R.; Liu, J.G. Assessing the potential of multispectral remote sensing for lithological mapping on the Antarctic Peninsula: Case study from eastern Adelaide Island, Graham Land. *Antarct. Sci.* **2010**, *22*, 299–318. [[CrossRef](#)]
25. van der Werff, H.; van der Meer, F. Sentinel-2 for Mapping Iron Absorption Feature Parameters. *Remote Sens.* **2015**, *7*, 12635–12653. [[CrossRef](#)]
26. van der Werff, H.; van der Meer, F. Sentinel-2A MSI and Landsat 8 OLI Provide Data Continuity for Geological Remote Sensing. *Remote Sens.* **2016**, *8*, 883. [[CrossRef](#)]
27. Ibrahim, E.; Barnabé, P.; Ramanaidou, E.; Pirarda, E. Mapping mineral chemistry of a lateritic outcrop in new Caledonia through generalized regression using Sentinel-2 and field reflectance spectra. *Int. J. Appl. Earth Obs. Geoinf.* **2018**, *73*, 653–665. [[CrossRef](#)]
28. El Ramly, M.F.; Greiling, R.O.; Rashwan, A.A.; Rasmy, A.H. Explanatory note to accompany the geological and structural maps of Wadi Hafafit area, Eastern Desert of Egypt. *Geol. Surv. Egypt* **1993**, *9*, 1–53.
29. Gabra, S.Z. Gold in Egypt. A commodity package: Minerals, petroleum and groundwater assessment program. USAID project 363-0105. *Geol. Surv. Egypt* **1986**.
30. El-Gaby, S.; List, F.K.; Tehrani, R. Geology, evolution and metallogenesis of the Pan-African Belt in Egypt. In *The Pan-African Belt of Northeast Africa and Adjacent Areas*; El Gaby, S., Greiling, R.O., Eds.; Friedrich Vieweg Sohn: Braunschweig, Germany, 1988; pp. 17–68.
31. Hussein, A.A. Mineral deposits. In *The Geology of Egypt: Rotterdam*; Said, R., Ed.; A.A. Balkema: Avereest, The Netherlands, 1990; pp. 511–566.
32. Botros, N.S. A new classification of the gold deposits of Egypt. *Ore Geol. Rev.* **2004**, *25*, 1–37. [[CrossRef](#)]
33. Zoheir, B.A. Characteristics and genesis of shear zone-related gold mineralization in Egypt: A case study from the Um El Tuyor mine, south Eastern Desert. *Ore Geol. Rev.* **2008**, *34*, 445–470. [[CrossRef](#)]



34. Zoheir, B.A. Structural controls, temperature-pressure conditions and fluid evolution of orogenic gold mineralisation in Egypt: A case study from the Betam gold mine, south Eastern Desert. *Miner. Depos.* **2008**, *43*, 79–95. [[CrossRef](#)]
35. Zoheir, B.A.; Lehmann, B. Listvenite–lode association at the Barramiya gold mine, Eastern Desert, Egypt. *Ore Geol. Rev.* **2011**, *39*, 101–115. [[CrossRef](#)]
36. Zoheir, B.A.; Weihed, P. Greenstone-hosted lode-gold mineralization at Dungash mine, Eastern Desert, Egypt. *J. Afr. Earth Sci.* **2014**, *99*, 165–187. [[CrossRef](#)]
37. Abd El-Wahed, M.A.; Harraz, H.Z.; El-Behairy, M.H. Transpressional imbricate thrust zones controlling gold mineralization in the Central Eastern Desert of Egypt. *Ore Geol. Rev.* **2016**, *78*, 424–446. [[CrossRef](#)]
38. Zoheir, B.A.; Emam, A.; Abd El-Wahed, M.; Soliman, N. Gold endowment in the evolution of the Allaqi-Heiani suture, Egypt: A synthesis of geological, structural, and space-borne imagery data. *Ore Geol. Rev.* **2019**, in press. [[CrossRef](#)]
39. Zoheir, B.A. Transpression zones in ophiolitic mélangé terranes: Potential exploration targets for gold in South Eastern Desert of Egypt. *J. Geochem. Explor.* **2011**, *111*, 23–38. [[CrossRef](#)]
40. Moore, J.M.M.; Shanti, A.M. The use of stress trajectory analysis in the elucidation of part of the Najd Fault System, Saudi Arabia. *Proc. Geol. Assoc.* **1973**, *84*, 383–403. [[CrossRef](#)]
41. Sultan, M.; Arvidson, R.E.; Duncan, I.J.; Stern, R.; El Kaliouby, B. Extension of the Najd Fault System from Saudi Arabia to the central Eastern Desert of Egypt based on integrated field and Landsat observations. *Tectonics* **1988**, *7*, 1291–1306. [[CrossRef](#)]
42. El Gaby, S.; List, F.K.; Tehrani, R. The basement complex of the Eastern Desert and Sinai. In *The Geology of Egypt*; Rushdi, S., Ed.; Balkema: Rotterdam, The Netherlands, 1990; pp. 175–184.
43. Ali-Bik, M.W.; Taman, Z.; El Kalioubi, B.; Abdel Wahab, W. Serpentine-hosted talc–magnesite deposits of Wadi Barramiya area, Eastern Desert, Egypt: Characteristics, petrogenesis and evolution. *J. Afr. Earth Sci.* **2012**, *64*, 77–89. [[CrossRef](#)]
44. Abd El-Wahed, M.A. Oppositely dipping thrusts and transpressional imbricate zone in the Central Eastern Desert of Egypt. *J. Afr. Earth Sci.* **2014**, *100*, 42–59. [[CrossRef](#)]
45. Abu El-Ela, A.M. Geology of Wadi Mubarak district, Eastern Desert, Egypt. Ph.D. Thesis, Tanta University, Tanta Chicago, IL, USA, 1985.
46. Zoheir, B.; Steele-MacInnis, M.; Garbe-Schönberg, D. Orogenic gold formation in an evolving, decompressing hydrothermal system: Genesis of the Samut gold deposit, Eastern Desert, Egypt. *Ore Geol. Rev.* **2019**, *105*, 236–257. [[CrossRef](#)]
47. Abdel-Karim, A.M.; El-Mahallawi, M.M.; Fringer, F. The Ophiolite Mélange of Wadi Dunqash and Wadi Arayis, Eastern Desert of Egypt: Petrogenesis and tectonic evolution. *Acta Mineral. Petrogr. (SzegedHung.)* **1996**, *47*, 129–141.
48. Aboelkhair, H.; Ninomiya, Y.; Watanabe, Y.; Sato, I. Processing and interpretation of ASTER TIR data for mapping of rare-metal-enriched albite granitoids in the Central Eastern Desert of Egypt. *J. Afr. Earth Sci.* **2010**, *58*, 141e151. [[CrossRef](#)]
49. Abu El-Rus, M.A.; Mohamed, M.A.; Lindh, A. Mueilha rare metals granite, Eastern Desert of Egypt: An example of a magmatic-hydrothermal system in the Arabian-Nubian Shield. *Lithos* **2017**, *294–295*, 362–382. [[CrossRef](#)]
50. Crawford, W.A.; Coulter, D.H.; Hubbard, H.B. The areal distribution, stratigraphy and major element chemistry of the Wadi Natash volcanic series, Eastern Desert, Egypt. *J. Afr. Earth Sci.* **1984**, *2*, 119–128. [[CrossRef](#)]
51. Mohamed, F.I.-I. The Natash alkaline volcanic field, Egypt: Geological and mineralogical inference on the evolution of a basalt to rhyolite eruptive suit. *J. Volcan Geotherm. Res.* **2001**, *105*, 291–322. [[CrossRef](#)]
52. Torres, R.; Snoeij, P.; Davidson, M.; Bibby, D.; Lokas, S. The Sentinel-1 mission and its application capabilities. *IEEE Int. Geosci. Remote Sens. Symp.* **2012**. [[CrossRef](#)]
53. Balzter, H.; Cole, B.; Thiel, C.; Schmullius, C. Mapping CORINE Land Cover from Sentinel-1A SAR and SRTM Digital Elevation Model Data using Random Forests. *Remote Sens.* **2015**, *7*, 14876–14898. [[CrossRef](#)]
54. Attema, E.; Bargellini, P.; Edwards, P.; Levrini, G.; Lokas, S.; Moeller, L.; Rosich-Tell, B.; Secchi, P.; Torres, R.; Davidson, M.; et al. Sentinel-1: The Radar Mission for GMES Operational Land and Sea Services. *Bulletin* **2007**, *131*, 10–17.
55. Igarashi, T. ALOS Mission requirement and sensor specification. *Adv. Space Res.* **2001**, *28*, 127–131. [[CrossRef](#)]

56. Rosenqvist, A.; Shimada, M.; Watanabe, M.; Tadono, T.; Yamauchi, K. Implementation of systematic data observation strategies for ALOS PALSAR, PRISM and AVNIR-2. In Proceedings of the 2004 IEEE International IEEE International Geoscience and Remote Sensing Symposium, Anchorage, AK, USA, 20–24 September 2004.
57. Earth Remote Sensing Data Analysis Center (ERSDAC). *PALSAR User's Guide*, 1st ed. 2019. Available online: [http://www.eorc.jaxa.jp/ALOS/en/doc/alos\\_userhb\\_en.pdf](http://www.eorc.jaxa.jp/ALOS/en/doc/alos_userhb_en.pdf) (accessed on 25 April 2019).
58. Drusch, M.; Del Bello, U.; Carlier, S.; Colin, O.; Fernandez, V.; Gascon, F.; Hoersch, B.; Isola, C.; Laberinti, P.; Martimort, P.; et al. Sentinel-2: ESA's optical high-resolution mission for GMES operational services. *Remote Sens. Environ.* **2012**, *120*, 25–36. [[CrossRef](#)]
59. van der Meer, F.D.; van der Werff, H.M.A.; van Ruitenbeek, F.J.A. Potential of ESA's Sentinel-2 for geological applications. *Remote Sens. Environ.* **2014**, *148*, 124–133. [[CrossRef](#)]
60. Sheng, Y.; Xia, Z.G. A comprehensive evaluation of filters for radar speckle suppression. In Proceedings of the 1996 International Geoscience and Remote Sensing Symposium, Lincoln, NE, USA, 31 May 1996; pp. 1559–1561.
61. Lee, J.-S. Digital Image Enhancement and Noise Filtering by Use of Local Statistics. *IEEE Trans. Pattern Anal. Mach. Intell.* **1980**, *2*, 165–168. [[CrossRef](#)] [[PubMed](#)]
62. Lopes, A.; Touzi, R.; Nezry, E. Adaptive speckle filter and scene heterogeneity. *IEEE Trans. Geosci. Remote Sens.* **1990**, *28*, 992–1000. [[CrossRef](#)]
63. Ben-Dor, E.; Kruse, F.A.; Lefkoff, A.B.; Banin, A. Comparison of three calibration techniques for the utilization of GER 63 channel scanner data of Makhtesh Ramon, Negev, Israel. *Photogramm. Eng. Remote Sens.* **1994**, *60*, 1339–1354.
64. Paganelli, F.; Grunsky, E.C.; Richards, J.P.; Pryde, R. Use of RADARSAT-1 principal component imagery for structural mapping: A case study in the Buffalo Head Hills area, northern central Alberta, Canada. *Can. J. Remote Sens.* **2003**, *29*, 111–140. [[CrossRef](#)]
65. Pal, S.K.; Majumdar, T.J.; Bhattacharya, A.K. ERS-2 SAR and IRS-1C LISS III data fusion: A PCA approach to improve remote sensing based geological interpretation. *ISPRS J. Photogramm. Remote Sens.* **2007**, *61*, 281–297. [[CrossRef](#)]
66. Cheng, Q.; Jing, L.; Panahi, A. Principal component analysis with optimum order sample correlation coefficient for image enhancement. *Int. J. Remote Sens.* **2006**, *27*, 3387–3401.
67. Gupta, R.P.; Tiwari, R.K.; Saini, V.; Srivastava, N. A simplified approach for interpreting principal component images. *Adv. Remote Sens.* **2013**, *2*, 111–119. [[CrossRef](#)]
68. Kalinowski, A.; Oliver, S. ASTER Mineral Index Processing Manual. Technical Report; 2004; Geoscience Australia. Available online: [http://www.ga.gov.au/image\\_cache/GA7833.pdf](http://www.ga.gov.au/image_cache/GA7833.pdf) (accessed on 1 June 2019).
69. Mars, J.C.; Rowan, L.C. Regional mapping of phyllic- and argillic-altered rocks in the Zagros magmatic arc, Iran, using Advanced Spaceborne Thermal Emission and Reflection Radiometer (ASTER) data and logical operator algorithms. *Geosphere* **2006**, *2*, 161–186. [[CrossRef](#)]
70. Abdelsalam, M.G.; Stern, R.J. Sutures and shear zones in the Arabian–Nubian Shield. *J. Afr. Earth Sci.* **1996**, *23*, 289–310. [[CrossRef](#)]
71. Abdelsalam, M.G.; Stern, R.J.; Copeland, P.; Elfaki, E.M.; Elhur, B.; Ibrahim, F.M. The Neoproterozoic Keraf Suture in Ne Sudan: Sinistral Transpression along the Eastern Margin of West Gondwana. *J. Geol.* **1998**, *106*, 133–148. [[CrossRef](#)]
72. Abdelsalam, M.G.; Abdeen, M.M.; Dwaidar, H.M.; Stern, R.J. Structural evolution of the Neoproterozoic western Allaqi-Heiani Suture, southeastern Egypt. *Precambrian Res.* **2003**, *124*, 87–104. [[CrossRef](#)]
73. Loizenbauer, J.; Wallbrecher, E.; Fntz, H.; Neumayr, P.; Khudeir, A.A.; Kloetzil, U. Structural geology, single zircon ages and fluid inclusion studies of the Meatiq metamorphic core complex. Implications for Neoproterozoic tectonics in the Eastern Desert of Egypt. *Precambrian Res.* **2001**, *110*, 357–383. [[CrossRef](#)]
74. Fritz, H.; Dalmeyer, D.R.; Wallbrecher, E.; Loizenbauer, J.; Hoinkes, G.; Neumayr, P.; Khudeir, A.A. Neoproterozoic tectonothermal evolution of the Central Eastern Desert, Egypt: A slow velocity tectonic process of core complex exhumation. *J. Afr. Earth Sci.* **2002**, *34*, 543–576. [[CrossRef](#)]
75. Shalaby, A.; Stüwe, K.; Makroum, F.; Fritz, H.; Kebede, T.; Klotzli, U. The Wadi Mubarak belt, Eastern Desert of Egypt: A Neoproterozoic conjugate shear system in the Arabian–Nubian Shield. *Precambrian Res.* **2005**, *136*, 27–50. [[CrossRef](#)]



76. Abd El-Wahed, M.A. Thrusting and transpressional shearing in the Pan-African nappe southwest El-Sibai core complex, Central Eastern Desert, Egypt. *J. Afr. Earth Sci.* **2008**, *50*, 16–36. [[CrossRef](#)]
77. Bailo, T.; Schandelmeier, H.; Franz, G.; Sun, C.-H.; Stern, R. Plutonic and metamorphic rocks from the Keraf Suture (NE Sudan): A glimpse of Neoproterozoic tectonic evolution on the NE margin of W. Gondwana. *Precambrian Res.* **2003**, *123*, 67–80. [[CrossRef](#)]
78. Klemm, R.; Klemm, D. *Gold and Gold Mining in Ancient Egypt and Nubia. Geoarchaeology of the Ancient Gold Mining in the Egyptian and Sudanese Eastern Deserts*; Springer Science & Business Media: Berlin/Heidelberg, Germany, 2013; 649p.
79. Sabet, A.H.; Tscogoev, V.B.; Bordonosov, V.P.; Badourin, L.M.; Zalata, A.A.; Francis, M.H. On Gold mineralization in the Eastern Desert of Egypt *Annals of the Geological. Surv. Egypt* **1976**, *6*, 201–212.
80. Osman, A. The mode of occurrence of gold-bearing listvenite at El Barramiya gold mine, Eastern desert, Egypt. Middle East Research Centre. Ain Shams University. *Earth Sci. Ser.* **1995**, *9*, 93–103.
81. Osman, A. The gold metallotect in the Eastern Desert of Egypt. In *Mineral Deposits at the Beginning of the 21st Century*; Piestrzyński, A., Pieczonka, J., A. Głuszek, A., Eds.; Swets & Zeitinger: Lisse, Belgium, 2001; pp. 795–798.
82. Helba, H.A.; Khalil, K.I.; Abdou, N.M. Alteration patterns related to hydrothermal gold mineralization in meta-andesites at Dungash area, Eastern Desert Egypt. *Resour. Geol.* **2001**, *51*, 19–30. [[CrossRef](#)]
83. Khalil, I.K.; Helba, H.A.; Mücke, A. Genesis of the gold mineralization at the Dungash gold mine area, Eastern Desert, Egypt: A mineralogical–microchemical study. *J. Afr. Earth Sci.* **2003**, *37*, 111–122. [[CrossRef](#)]
84. Hassan, M.M.; Soliman, M.M.; Azzaz, S.A.; Attawiya, M.Y. Geological studies on gold mineralization at Sukkari, Um Ud, and Samut, Eastern Desert, Egypt. *Ann. Geol. Surv. Egypt* **1990**, *16*, 89–95.
85. Dewey, J.E.; Holdsworth, R.E.; Strachan, R.A. Transpression and transtension zones. In *Continental Transpressional and Transtensional Tectonics. Geological Society*; Holdsworth, R.E., Strachan, R.A., Dewey, J.E., Eds.; Special Publications: London, UK, 1998; Volume 135, pp. 1–14.
86. Goldfarb, R.J.; Taylor, R.D.; Collins, G.S.D.; Goryachev, N.A.; Orlandini, O.F. Phanerozoic continental growth and gold metallogeny of Asia. *Gondwana Res.* **2014**, *25*, 48–102. [[CrossRef](#)]
87. Harland, W.B. Tectonic transpression in Caledonian Spitsbergen. *Geol. Mag.* **1971**, *108*, 27–42. [[CrossRef](#)]
88. Fossen, H.; Tikoff, B.; Teyssier, C.T. Strain modeling of transpressional and transtensional deformation. *Nor. Geol. Tidsskrift* **1994**, *74*, 134–145.
89. Jones, R.R.; Holdsworth, R.E.; Clegg, P.; McCaffrey, K.; Travarnelli, E. Inclined transpression. *J. Struct. Geol.* **2004**, *30*, 1531–1548. [[CrossRef](#)]
90. Sarkarinejad, K.; Faghih, A.; Grasemann, B. Transpressional deformations within the Sanandaj–Sirjan metamorphic belt (Zagros Mountains, Iran). *J. Struct. Geol.* **2008**, *30*, 818–826. [[CrossRef](#)]
91. Abd El-Wahed, M.A.; Ashmawy, M.H.; Tawfik, H.A. Structural setting of Cretaceous pull-apart basins and Miocene extensional folds in Quseir-Umm Gheig region, northwestern Red Sea, Egypt. *Lithosphere* **2010**, *2*, 13–32. [[CrossRef](#)]
92. Abd El-Wahed, M.A.; Kamh, S.; Ashmawy, M.; Shebl, A. Transpressive Structures in the Ghadir Shear Belt, Eastern Desert, Egypt: Evidence for Partitioning of Oblique Convergence in the Arabian–Nubian Shield during Gondwana Agglutination. *Acta Geol. Sin.-Engl. Ed.* **2019**. [[CrossRef](#)]
93. Abd El-Wahed, M.A.; Kamh, S.Z. Pan African dextral transpressive duplex and flower structure in the Central Eastern Desert of Egypt. *Gondwana Res.* **2010**, *18*, 315–336. [[CrossRef](#)]
94. Abd El-Wahed, M.A.; Kamh, S.Z. Evolution of conjugate strike-slip duplexes and wrench-related folding in the Central part of Al Jabal Al Ahkdar, NE Libya. *J. Geol.* **2013**, *121*, 173–195. [[CrossRef](#)]
95. Li, S.; Wilde, S.A.; Wanga, T.; Guo, Q. Latest Early Permian granitic magmatism in southern Inner Mongolia, China: Implications for the tectonic evolution of the southeastern Central Asian Orogenic Belt. *Gondwana Res.* **2016**, *29*, 168–180. [[CrossRef](#)]
96. Zaw, K.; Meffre, S.; Lai, C.K.; Burrett, C.; Santosh, M.; Graham, I.; Manaka, T.; Salam, A.; Kamvong, T.; Cromie, P. Tectonics and metallogeny of mainland Southeast Asia -A review and contribution. *Gondwana Res.* **2014**, *26*, 5–30.
97. Hedenquist, J.W.; Thompson, J.F.H.; Goldfarb, R.J.; Richards, J.P. Distribution, character, and genesis of gold deposits in metamorphic terranes. In *Economic geology one hundredth anniversary volume 1905–2005*; Hedenquist, J.W.; Thompson, J.F.H.; Goldfarb, R.J.; Richards, J.P. Society of Economic Geologists: Littleton, CO, USA, 2005; pp. 407–450.

98. Reinhardt, M.C.; Davison, I. Structural and lithological controls on gold deposition in the shear zone-hosted Fazenda Brasileiro Mine, Bahia state, Northeast Brazil. *Econ. Geol.* **1990**, *85*, 952–967. [[CrossRef](#)]
99. Almond, D.C.; Shaddad, M.Z. Setting of gold mineralization in the northern Red Sea Hills of Sudan. *Econ. Geol.* **1984**, *79*, 389–392. [[CrossRef](#)]
100. El-Samani, Y.; Al-Muslem, A.; El Tokhi, M. Geology and geotectonic classification of Pan-African gold mineralizations in the Red Sea Hills, Sudan. *Int. Geol. Rev.* **2001**, *43*, 1117–1128. [[CrossRef](#)]
101. Zoheir, B.A.; El-Shazly, A.K.; Helba, H.; Khalil, K.I.; Bodnar, R.J. Origin and evolution of the Um Egat and Dungash orogenic gold deposits, Egyptian eastern desert: Evidence from fluid inclusions in quartz. *Econ. Geol.* **2008**, *103*, 405–424. [[CrossRef](#)]
102. Murr, A. Geologische Kartierung der Goldlagerstättenbezirke Fatira und Dungash in der Ostwüste Ägyptens. unpubl. Master thesis, LMUUniversity, Munich, Germany, 1994.



© 2019 by the authors. Licensee MDPI, Basel, Switzerland. This article is an open access article distributed under the terms and conditions of the Creative Commons Attribution (CC BY) license (<http://creativecommons.org/licenses/by/4.0/>).